

Accurate Tracking of Aggressive Quadrotor Trajectories using Incremental Nonlinear Dynamic Inversion and Differential Flatness

Ezra Tal

Sertac Karaman

Abstract— Autonomous unmanned aerial vehicles (UAVs) that can execute aggressive (*i.e.*, high-speed and high-acceleration) maneuvers have attracted significant attention in the past few years. In this paper, we propose a novel control law for accurate tracking of aggressive quadcopter trajectories. The proposed method tracks position and yaw angle with their derivatives of up to fourth order, specifically, the position, velocity, acceleration, jerk, and snap along with the yaw angle, yaw rate and yaw acceleration. Two key aspects of the proposed method are the following. First, the controller exploits the *differential flatness* of the quadcopter dynamics to generate feedforward inputs for attitude rate and attitude acceleration in order to track the jerk and snap references. The tracking is enabled by direct control of body torque using closed-loop control of all four propeller speeds based on optical encoders attached to the motors. Second, the controller utilizes the *incremental nonlinear dynamic inversion* (INDI) method for accurate tracking of linear and angular accelerations despite external disturbances. Hence, no prior modeling of aerodynamic effects is required. We rigorously analyze the proposed controller through response analysis, and we demonstrate it in experiments. The proposed control law enables a 1-kg quadcopter UAV to track complex 3D trajectories, reaching speeds up to 8.2 m/s and accelerations up to 2g, while keeping the root-mean-square tracking error down to 4 cm, in a flight volume that is roughly 6.5 m long, 6.5 m wide, and 1.5 m tall. We also demonstrate the robustness of the controller by attaching a drag plate to the UAV in flight tests and by pulling on the UAV with a rope during hover.

SUPPLEMENTAL MATERIAL

A video of the experiments can be found at <https://youtu.be/M1LE9M1FmVA>.

I. INTRODUCTION

High-speed aerial navigation through complex environments has been a focus of control theory and robotics research for decades. More recently, *drone racing* events, at which remotely-operated rotary-wing aircraft are piloted through challenging obstacle courses at very high speeds, have further inspired and popularized this research direction.

Accurate control of the aircraft during aggressive maneuvers is essential towards enabling fully-autonomous drone racers. Control design for rotary-wing, vertical take-off and landing (VTOL) aircraft at low speeds typically neglects aerodynamics. However, at high speeds, the aerodynamic drag — which is hard to model — becomes a dominant factor. Accounting for aerodynamics is an important challenge in control design for vehicles operating at high speeds.

E. Tal and S. Karaman are with the Department of Aeronautics and Astronautics and the Laboratory for Information and Decision Systems, Massachusetts Institute of Technology (MIT), Cambridge, MA 02139, USA. {eatal, sertac}@mit.edu

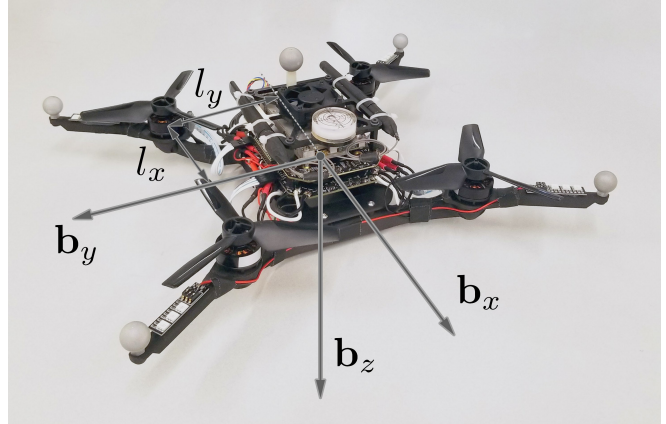


Fig. 1: Quadrotor with body-fixed reference system and moment arm definitions.

In this paper, we propose a control system for accurate trajectory tracking during aggressive maneuvering of quadcopter aircraft, such as the one shown in Figure 1. The controller exploits the differential flatness of the quadcopter dynamics to generate feedforward control commands, and it relies on incremental nonlinear dynamic inversion (INDI) to handle external disturbances, *e.g.*, aerodynamic drag forces.

Feedback linearization [1]–[3], also called nonlinear dynamic inversion (NDI), enables the use of a linear control law by transforming the nonlinear dynamics into a linear input-output map. Although variants of feedback linearization were quickly developed for flight control [4]–[8], it is well known that exact dynamic inversion inherently suffers from lack of robustness [9]. As a result, other nonlinear control methods, *e.g.*, adaptive sliding mode [9]–[11] and backstepping designs [12], have been considered in order to achieve robustness in flight control. More recently, an incremental version of nonlinear dynamic inversion has been developed [13], [14], based on earlier derivations [15], [16], which provide robustness by incrementally applying control inputs based on inertial measurements. The INDI technique has been applied to quadcopters for stabilization, *e.g.*, for robust hovering [17], [18], but not for trajectory tracking.

The differential flatness property allows expressing all states and inputs of a dynamic system in terms of a set of flat outputs and its derivatives [19]–[21]. In the context of flight control, this property enables reformulation of the trajectory tracking problem as a state tracking problem [8], [22], which has also been applied to quadcopter trajectory tracking [23]–[26].

Quadcopter aircraft are relatively easy to maneuver and experiment with. Arguably, these qualities make them ideal

for drone racing events. For the same reasons, they have been heavily used as experimental platforms in robotics and control theory research since the start of this century [27]–[30]. Complex trajectory tracking control systems have been designed and demonstrated for aircraft in motion capture rooms, where the position and the orientation of the aircraft can be obtained with high accuracy [31]–[37]. Agile maneuvers for quadcopter aircraft have also been demonstrated [38], [39]. Despite being impressive, these demonstrations have showcased complex trajectories only at relatively slow speeds, *e.g.*, less than 2 m/s, so that aerodynamic forces and moments may be neglected. At higher speeds, aerodynamic effects heavily influence the vehicle dynamics. Recent research has considered the modeling [26], [40], [41], estimation [42], [43], and learning [44] of aerodynamic drag effects towards tracking control for high-speed trajectories.

The main contribution of this paper is a trajectory tracking control design that achieves accurate tracking during high-speed and high-acceleration maneuvers without depending on modeling or estimation of aerodynamic drag parameters. The design exploits differential flatness of the quadcopter dynamics to generate feedforward control terms based on the reference trajectory and its derivatives up to fourth order, *i.e.*, velocity, acceleration, jerk, and snap. Modeling inaccuracies and disturbances due to aerodynamic drag are compensated for using incremental control based on the INDI technique. This control design is novel in the following ways. Firstly, we develop a new control methodology that enables the tracking of snap by accurately controlling motor speeds using optical encoders attached to the motors. We recognize that snap is directly related to vehicle angular accelerations, which can be tracked by direct application of body torque commands. This is made possible by precise closed-loop control of the motor speeds using measurements from the optical encoders attached to each motor. To the best of our knowledge, the direct control over snap using motor speed measurements is novel. In contrast, trajectory tracking control based on body rate inputs — *e.g.*, using a typical inner-loop flight controller — is incapable of truly considering reference snap. Secondly, we develop a novel INDI control design for quadcopter trajectory tracking, in which thrust and torque commands are applied incrementally for robustness against significant external disturbances, such as aerodynamic drag. To the best of the our knowledge, the proposed controller is the first design that is tailored for trajectory tracking, as existing INDI control designs focus on state regulation, *e.g.*, for maintaining hover under external disturbances. Thirdly, we provide and evaluate a novel implementation of INDI angular acceleration control that includes nonlinear computation of the control increments, as opposed to the existing implementations that use inversion of linearized control effectiveness equations. Finally, we demonstrate the proposed controller in experiments, and we rigorously analyze the benefits of the key aspects of our controller through response analysis. In our experiments, the proposed control law enables a 1-kg UAV to track complex 3D trajectories, reaching speeds up to 8.2 m/s and accelerations up to 2g, while keeping the

root-mean-square tracking error down to 4 cm, in a flight volume that is roughly 6.5 m long, 6.5 m wide, and 1.5 m tall. We also demonstrate the robustness of the controller in experiments by attaching a drag plate to the UAV in flight tests and by pulling on the UAV using a tensioned wire during hover. The improved performance due to the tracking of reference jerk and snap through feedforward angular velocity and angular acceleration inputs is also demonstrated both in theoretical analysis and in experiments.

The paper is structured as follows: Nomenclature is presented in Table I. In Section II, the quadrotor model is specified, and we show how feedforward control inputs are formulated in terms of the reference trajectory using differential flatness. In Section III, we describe the architecture of the trajectory tracking controller, and its individual components. Section IV illustrates the robustness of INDI and the effect of the feedforward control inputs through response analysis. Finally, we give experimental results from real-life flights in Section V. Additionally, we provide the full derivation of differential flatness properties in Appendix I, and the full derivation of the NDI attitude controller in Appendix II.

II. PRELIMINARIES

In this section, we describe the quadrotor dynamics model, and its differential flatness property. Specifically, we show how this property is utilized to derive attitude rate and attitude acceleration references that will be employed as feedforward control inputs by the trajectory tracking controller.

A. Quadrotor Model

We consider a 6 degree-of-freedom (DOF) quadrotor, as shown in Fig. 1. The unit vectors depicted in the figure are the basis of the body-fixed reference frame and form the rotation matrix $\mathbf{R} = [\mathbf{b}_x \ \mathbf{b}_y \ \mathbf{b}_z] \in SO(3)$, which gives the transformation from the body-fixed reference frame to the inertial reference frame. The basis of the north-east-down (NED) inertial reference frame consists of the columns of the identity matrix $\mathbf{I} = [\mathbf{i}_x \ \mathbf{i}_y \ \mathbf{i}_z]$.

The vehicle translational dynamics are given by

$$\dot{\mathbf{x}} = \mathbf{v}, \quad (1)$$

$$\dot{\mathbf{v}} = g\mathbf{i}_z + \tau\mathbf{b}_z + m^{-1}\mathbf{f}_{ext}, \quad (2)$$

where \mathbf{x} and \mathbf{v} are the position and velocity in the inertial reference frame, respectively. Equation (2) includes three contributions to the linear acceleration. Firstly, the gravitational acceleration g in downward direction. Secondly, the specific thrust τ , which is the ratio of the total thrust T and the vehicle mass m . Note that the thrust vector is always aligned with the \mathbf{b}_z -axis, so that the quadrotor must pitch or roll to accelerate forward, backward or sideways. Finally, the external disturbance force vector \mathbf{f}_{ext} accounts for all other forces acting on the vehicle, such as aerodynamic drag.

The rotational dynamics are given by

$$\dot{\boldsymbol{\xi}} = \mathbf{S}\boldsymbol{\Omega}, \quad (3)$$

$$\dot{\boldsymbol{\Omega}} = \mathbf{J}^{-1}(\boldsymbol{\mu} + \boldsymbol{\mu}_{ext} - \boldsymbol{\Omega} \times \mathbf{J}\boldsymbol{\Omega}), \quad (4)$$

TABLE I: Nomenclature. The subscript *ref* is used to indicate elements of the reference trajectory function and its time derivatives, as well as feedforward variables directly obtained from the reference trajectory function. The subscript *c* is used for commanded values that are obtained from a feedback control loop. Low-pass filtered measurements and signals obtained from such measurements are indicated by the subscript *f*.

| | | | |
|---|--|--------------------|--|
| $\circ n$ | n -th Hadamard (element-wise) power | NI | transfer function corresponding to nonincremental controller |
| $[\bullet]_x$ | cross-product matrix | p | vehicle roll rate around \mathbf{b}_x -axis, rad/s |
| $\mathbf{0}$ | vector or matrix of zeros | p | polynomial relating ESC input and motor speed |
| \mathbf{a} | linear acceleration in inertial frame, m/s ² | q | vehicle pitch rate around \mathbf{b}_y -axis, rad/s |
| \mathbf{a}^b | linear acceleration including gravitational acceleration in body-fixed frame, <i>i.e.</i> , as measured by IMU, m/s ² | r | vehicle yaw rate around \mathbf{b}_z -axis, rad/s |
| \mathbf{b}_x | first basis vector of body-fixed frame | \mathbf{R} | body-fixed to inertial frame rotation matrix |
| \mathbf{b}_y | second basis vector of body-fixed frame | \mathbb{R} | set of real numbers |
| \mathbf{b}_z | third basis vector of body-fixed frame | s | abbreviation for sin |
| B | one-sample backshift operator | S | Laplace variable |
| c | abbreviation for cos | \mathbf{s} | snap in inertial frame, m/s ⁴ |
| C^n | n -th order differentiability class | \mathbf{S} | body-fixed angular rate to attitude derivative transformation matrix |
| f | attitude kinematics function | $SO(3)$ | three-dimensional special orthogonal group |
| \mathbf{f}_{ext} | external disturbance force vector, N | t | abbreviation for tan |
| g | gravitational acceleration, 9.81 m/s | t | time, s |
| g | attitude kinematics input function | T | thrust, N |
| \mathbf{G}_1 | propeller speed control effectiveness matrix | \mathbb{T} | circle group |
| \mathbf{G}_2 | propeller acceleration control effectiveness matrix | \mathbf{u} | feedback component of virtual attitude control input, rad/s ² |
| h | attitude kinematics output function | $\bar{\mathbf{u}}$ | virtual attitude control input, rad/s ² |
| $H(s)$ | low-pass filter transfer function | \mathbf{v} | velocity in inertial frame, m/s |
| \mathbf{I} | 3×3 identity matrix | \mathbf{x} | position in inertial frame, m |
| \mathbf{i}_x | first standard basis vector | α | vehicle pitch acceleration around \mathbf{b}_y -axis, rad/s ² |
| \mathbf{i}_y | second standard basis vector | Δ | modeling error parameter |
| \mathbf{i}_z | third standard basis vector | Δt | motor speed controller time interval, s |
| j | jerk in inertial frame, m/s ³ | ζ | ESC pulse width modulation command vector |
| \mathbf{J} | vehicle moment of inertia matrix, kg·m ² | θ | vehicle pitch angle, rad |
| J_{yy} | vehicle moment of inertia around \mathbf{b}_y -axis, kg·m ² | μ | control moment vector, N·m |
| J_{rz} | motor rotor and propeller moment of inertia, kg·m ² | μ_{ext} | external disturbance moment vector, N·m |
| $k_\xi, k_{\dot{\xi}}$ | scalar control gains | ξ | roll-pitch-yaw Euler attitude vector, rad |
| k_G | linearized pitch control effectiveness, kg·m ² /(rad·s) | $\sigma_{ref}(t)$ | reference trajectory function |
| k_{μ_z} | propeller torque coefficient, kg·m ² /rad ² | τ | specific thrust, m/s ² |
| k_τ | propeller thrust coefficient, kg·m/rad ² | τ_m | motor-ESC-control model time constant |
| $\mathbf{K}_x, \mathbf{K}_v$ | diagonal control gain matrices | ϕ | vehicle roll angle, rad |
| $\mathbf{K}_a, \mathbf{K}_\xi$ | | χ | vehicle attitude and angular rate vector |
| $\mathbf{K}_\dot{\xi}, \mathbf{K}_\omega$ | | ψ | vehicle yaw angle, rad |
| l_x | moment arm component parallel to \mathbf{b}_x -axis, m | ω | deviation from hover state motor rotation speed, rad/s |
| l_y | moment arm component parallel to \mathbf{b}_z -axis, m | ω_0 | hover state motor rotation speed, rad/s |
| L^n | n -th Lie derivative | ω | vector of motor rotation speeds around \mathbf{b}_z -axis, rad/s |
| m | vehicle mass, kg | Ω | vehicle angular rate vector, rad/s |
| $M(s)$ | ESC, motor control, and motor dynamics transfer function | | |

where $\xi = [\phi \ \theta \ \psi]^T$ is the roll-pitch-yaw Euler attitude vector, and $\Omega = [p \ q \ r]^T$ is the angular velocity in the body-fixed reference frame. The attitude rate and angular velocity are related by the following transformation matrix:

$$\mathbf{S} = \begin{bmatrix} 1 & \sin \phi \tan \theta & \cos \phi \tan \theta \\ 0 & \cos \phi & -\sin \phi \\ 0 & \frac{\sin \phi}{\cos \theta} & \frac{\cos \phi}{\cos \theta} \end{bmatrix}. \quad (5)$$

The matrix \mathbf{J} is the vehicle moment of inertia tensor. The control moment vector is indicated by μ , and the external disturbance moment vector by μ_{ext} . The third term of (4) accounts for the conservation of angular momentum in the rotating body-fixed reference frame.

The body-to-inertial transformation matrix \mathbf{R} can be obtained from the vehicle attitude ξ as follows:

$$\mathbf{R} = \begin{bmatrix} c\psi c\theta & -s\psi c\phi + c\psi s\theta s\phi & s\psi s\phi + c\psi s\theta c\phi \\ s\psi c\theta & c\psi c\phi + s\psi s\theta s\phi & -c\psi s\phi + s\psi s\theta c\phi \\ -s\theta & c\theta s\phi & c\theta c\phi \end{bmatrix} \quad (6)$$

with c denoting cos and s denoting sin.

The total thrust T and control moment vector in body-reference frame μ are a function of the vector of rotor speeds ω according to

$$\begin{bmatrix} \mu \\ T \end{bmatrix} = \mathbf{G}_1 \omega^\circ + \mathbf{G}_2 \dot{\omega}, \quad (7)$$

where \circ indicates the Hadamard power,

$$\mathbf{G}_1 = \begin{bmatrix} l_y k_\tau & -l_y k_\tau & -l_y k_\tau & l_y k_\tau \\ l_x k_\tau & l_x k_\tau & -l_x k_\tau & -l_x k_\tau \\ -k_{\mu_z} & k_{\mu_z} & -k_{\mu_z} & k_{\mu_z} \\ -k_\tau & -k_\tau & -k_\tau & -k_\tau \end{bmatrix}, \quad (8)$$

with l_x and l_y the moment arms indicated in Fig. 1, k_τ the motor thrust coefficient and k_{μ_z} the motor torque coefficient, and

$$\mathbf{G}_2 = \begin{bmatrix} 0 & 0 & 0 & 0 \\ 0 & 0 & 0 & 0 \\ -J_{rz} & J_{rz} & -J_{rz} & J_{rz} \\ 0 & 0 & 0 & 0 \end{bmatrix} \quad (9)$$

with J_{r_z} the rotor and propeller moment of inertia. We only consider the z -component of the rotor speed, *i.e.*, ω is a four-element vector where each element represents the rotation rate about the b_z -axis of one of the four motors. Additional gyroscopic contributions are relatively small and may be neglected [17].

B. Differential Flatness

In this section, we show how attitude rate and attitude acceleration references are formulated in terms of the reference trajectory. For brevity, we only state key results that are applied in the trajectory tracking control. A full derivation is given in Appendix I.

The differential flatness property enables us to express reference states as a function of the four flat outputs (and their derivatives) given by the reference trajectory function [45]:

$$\boldsymbol{\sigma}_{ref}(t) = [\mathbf{x}_{ref}(t)^T \ \psi_{ref}(t)]^T, \quad (10)$$

which consists of the quadrotor position in the inertial reference frame $\mathbf{x}_{ref}(t) \in \mathbb{R}^3$, and the vehicle yaw angle $\psi_{ref}(t) \in \mathbb{T}$, where \mathbb{T} denotes the circle group. For convenience, we do not explicitly write the time argument t everywhere. We assume that \mathbf{x}_{ref} is of differentiability class C^4 , *i.e.*, its first four derivatives exist and are continuous, and that ψ_{ref} is of class C^2 . By successive differentiation of \mathbf{x}_{ref} , we obtain the reference velocity \mathbf{v}_{ref} , the reference acceleration \mathbf{a}_{ref} , the reference jerk \mathbf{j}_{ref} , and the reference snap \mathbf{s}_{ref} . All in the inertial reference frame. Similarly, we obtain references for the yaw rate $\dot{\psi}_{ref}$, and the yaw acceleration $\ddot{\psi}_{ref}$ by differentiation of ψ_{ref} .

We denote reference states — directly obtained from the reference trajectory — with the same subscript, *i.e.*, ref . The reference states for angular rate and angular acceleration will be applied as feedforward inputs in the trajectory tracking control design.

By taking the derivative of (2), we obtain the following expression for the jerk:

$$\mathbf{j} = \tau \mathbf{R} [\mathbf{i}_z]_\times^T \mathbf{S}^{-1} \dot{\boldsymbol{\xi}} + \dot{\tau} \mathbf{b}_z, \quad (11)$$

where $[\bullet]_\times$ indicates the cross-product matrix. Equation (11) shows that the jerk is affine in $\dot{\boldsymbol{\xi}}$. Thus, the relation can be inverted to obtain the expression

$$\dot{\boldsymbol{\xi}}_{ref} = \frac{1}{\tau} \begin{bmatrix} -\mathbf{b}_y^T \\ \mathbf{b}_x^T / \cos \phi \\ 0 \end{bmatrix} \mathbf{j}_{ref} + \dot{\psi}_{ref} \begin{bmatrix} \sin \theta \\ -\cos \theta \tan \phi \\ 1 \end{bmatrix}, \quad (12)$$

which gives the reference attitude rate $\dot{\boldsymbol{\xi}}_{ref}$ as a function of \mathbf{j}_{ref} and $\dot{\psi}_{ref}$. We note that \mathbf{f}_{ext} is considered constant here, as its dynamics are unmodeled.

To obtain the attitude accelerations $\ddot{\phi}_{ref}$ and $\ddot{\theta}_{ref}$, we first compute the derivative of (11):

$$\mathbf{s} = \mathbf{R} \left(\ddot{\tau} \mathbf{i}_z + (2\dot{\tau} + \tau [\Omega]_\times) [\mathbf{i}_z]_\times^T \Omega + \tau [\mathbf{i}_z]_\times^T \dot{\Omega} \right), \quad (13)$$

where (by taking the derivative of (3))

$$\dot{\Omega} = -\mathbf{S}^{-1} \dot{\mathbf{S}} \Omega + \mathbf{S}^{-1} \ddot{\boldsymbol{\xi}} \quad (14)$$

with

$$\dot{\mathbf{S}} = \dot{\phi} \begin{bmatrix} 0 & c\phi t\theta & -s\phi t\theta \\ 0 & -s\phi & -c\phi \\ 0 & \frac{c\phi}{\cos \theta} & -\frac{s\phi}{c\theta} \end{bmatrix} + \dot{\theta} \begin{bmatrix} 0 & -\frac{s\phi}{s^2\theta-1} & \frac{c\phi}{c^2\theta} \\ 0 & 0 & 0 \\ 0 & -\frac{s\phi s\theta}{s^2\theta-1} & \frac{c\phi s\theta}{c^2\theta} \end{bmatrix} \quad (15)$$

and t indicating tan. Hence, (13) is affine in $\ddot{\boldsymbol{\xi}}$, and by inversion we obtain the following expression for the reference attitude acceleration $\ddot{\boldsymbol{\xi}}_{ref}$ in terms of \mathbf{s}_{ref} and $\dot{\psi}_{ref}$:

$$\ddot{\boldsymbol{\xi}}_{ref} = \frac{1}{\tau} \begin{bmatrix} -\mathbf{b}_y^T \\ \mathbf{b}_x^T / \cos \phi \\ 0 \end{bmatrix} \mathbf{s}_{ref} + \ddot{\psi}_{ref} \begin{bmatrix} \sin \theta \\ -\cos \theta \tan \phi \\ 1 \end{bmatrix} - \begin{bmatrix} 1 & 0 & 0 \\ 0 & 1 & 0 \\ 0 & 0 & 0 \end{bmatrix} \mathbf{C}^{-1} \mathbf{e} \quad (16)$$

with

$$\mathbf{C} = \begin{bmatrix} \tau (c\phi s\psi - c\psi s\phi \theta) & \tau c\phi c\psi c\theta & s\psi s\phi + c\psi s\theta c\phi \\ -\tau (c\phi c\psi + s\phi s\psi \theta) & \tau c\phi c\theta s\psi & -c\psi s\phi + s\psi s\theta c\phi \\ -\tau c\theta s\phi & -\tau c\phi s\theta & c\theta c\phi \end{bmatrix} \quad (17)$$

and

$$\mathbf{e} = \mathbf{R} \left((2\dot{\tau} + \tau [\Omega]_\times) [\mathbf{i}_z]_\times^T \Omega - \tau [\mathbf{i}_z]_\times^T \mathbf{S}^{-1} \dot{\mathbf{S}} \Omega \right). \quad (18)$$

III. TRAJECTORY TRACKING CONTROL

The proposed controller aims to accurately follow the reference trajectory $\boldsymbol{\sigma}_{ref}$ by tracking not only the position and yaw references, but also their derivatives up to the fourth order. As shown in Section II-B, reference states are obtained from the high-order derivatives using the differential flatness property of the quadrotor dynamics. These reference states are used as feedforward control inputs in the trajectory tracking control.

The resulting control design consists of several components based on various control methods. Table II gives an overview of the components with their respective control methods, references, and control outputs. The control architecture is visualized in three block diagrams. Figure 2 shows the *Proportional-Derivative (PD) Position and Velocity Controller* as described in Section III-A. Its output — the acceleration command — serves as input to the *INDI Linear Acceleration Controller*, which is shown in Fig. 3 and described in Section III-B. The *NDI Attitude and Attitude Rate Controller* described in Section III-C, and the *INDI Angular Acceleration Controller* described in Section III-D are also shown in Fig. 3. The resulting thrust and control moment commands are the inputs of the *Inversion-Based Moment and Thrust Controller*, which in turn computes the motor speed reference for the *Integrative Motor Speed Controller*. Both of these controllers are shown in Fig. 4 and described in Section III-E. The motor speed controller communicates directly with the ESCs through its pulse width modulation (PWM) output signals.

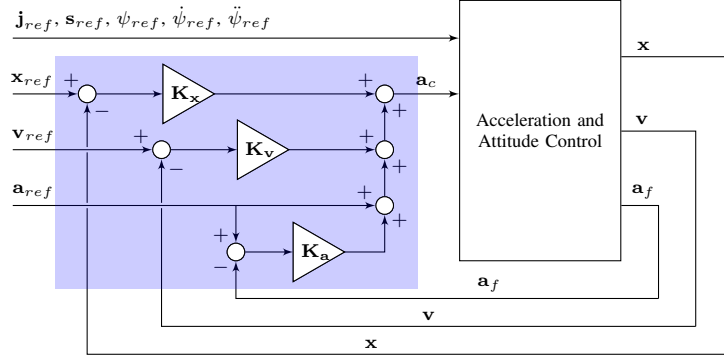


Fig. 2: Position and Velocity Control. The blue area contains the PD control design as described in Section III-A.

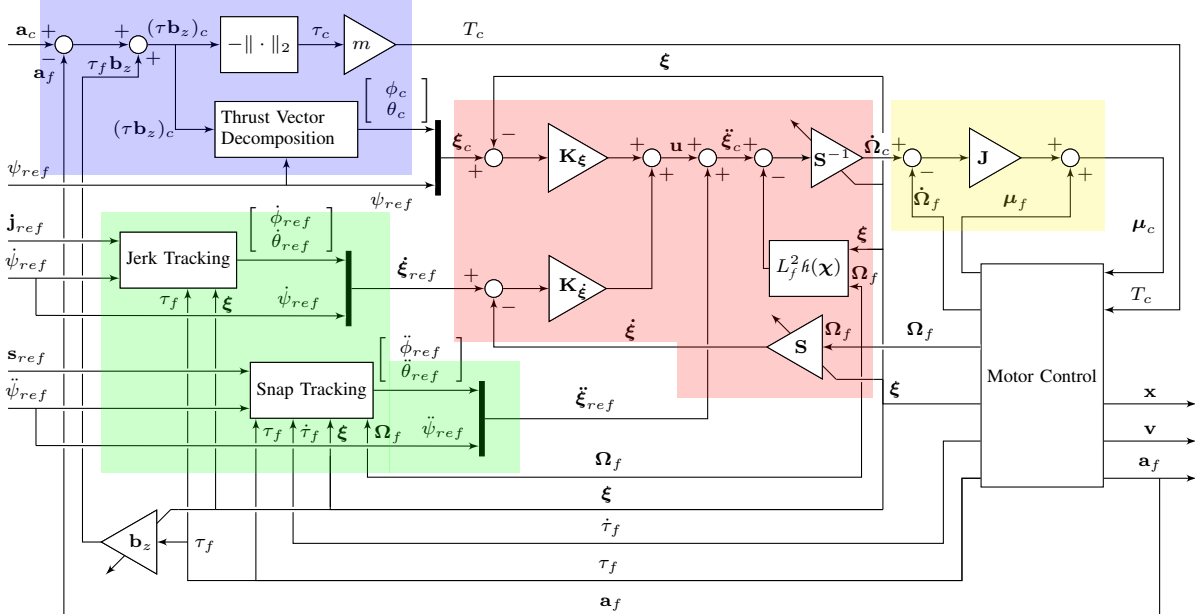


Fig. 3: Acceleration and Attitude Control. The blue area contains the INDI linear acceleration control as described in Section III-B. *Thrust Vector Decomposition* refers to the computation given in (26) and (27). The green area contains the computation of attitude rate and attitude acceleration references based on differential flatness as described in Section II-B. The red area contains the NDI attitude and attitude rate control as described in Section III-C. The yellow area contains the INDI angular acceleration control as described in Section III-D.

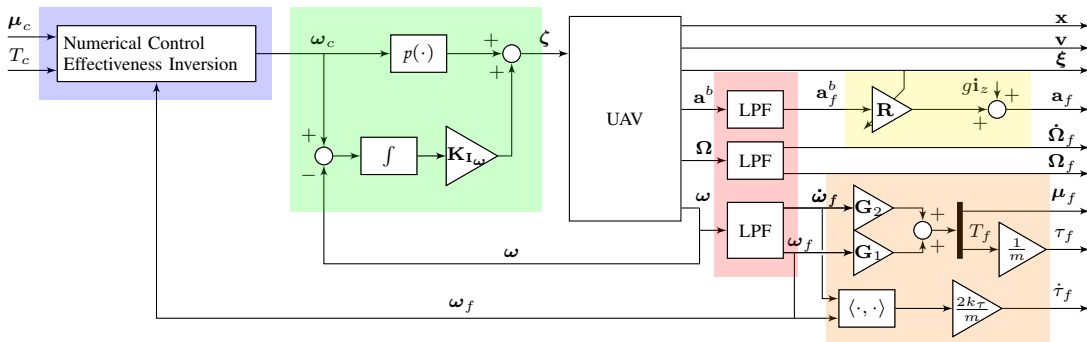


Fig. 4: Motor Control and Computation of Filtered Signals. The blue and green areas contain the moment and thrust control, and the motor speed control, respectively. Both are described in Section III-E. *Numerical Control Effectiveness Inversion* refers to the inversion of (39). The *UAV* block represents the UAV hardware, including ESCs, motors, and sensors. The red area contains the LPFs used to filter the IMU and motor speed measurements. The yellow area contains the computation of the gravity-corrected acceleration in the inertial reference frame, according to (19). The orange block contains the computation of the control moment, thrust, and thrust derivative based on the filtered motor speed measurements, according to (7).

TABLE II: Overview of trajectory tracking controller components.

| Component | Methodology | Reference | Control Output | Description |
|------------------------------------|-----------------------|---|-------------------------------------|---------------|
| Position and Velocity Control | PD | $\mathbf{x}_{ref}, \mathbf{v}_{ref}, \mathbf{a}_{ref}$ | \mathbf{a}_c | Section III-A |
| Linear Acceleration Control | INDI | \mathbf{a}_c | ϕ_c, θ_c, T_c | Section III-B |
| Jerk and Snap Tracking | Differential Flatness | $\mathbf{j}_{ref}, s_{ref}, \dot{\psi}_{ref}, \ddot{\psi}_{ref}$ | $\dot{\xi}_{ref}, \ddot{\xi}_{ref}$ | Section II-B |
| Attitude and Attitude Rate Control | NDI | $\phi_c, \theta_c, \psi_{ref}, \dot{\xi}_{ref}, \ddot{\xi}_{ref}$ | $\dot{\Omega}_c$ | Section III-C |
| Angular Acceleration Control | INDI | $\dot{\Omega}_c$ | μ_c | Section III-D |
| Moment and Thrust Control | Inversion | μ_c, T_c | ω_c | Section III-E |
| Motor Speed Control | Integrative | ω_c | ζ | Section III-E |

In order to apply INDI linear and angular acceleration control, the current accelerations are obtained through accelerometer measurements and differentiated gyroscope measurements [13]. The IMU signals are filtered using a digital second-order Butterworth low-pass filter (LPF) to alleviate the effects of airframe vibrations and other noise sources. We denote the LPF linear acceleration output (in body-fixed reference frame) \mathbf{a}_f^b , and the LPF angular rate output $\dot{\Omega}_f$. The derivative $\dot{\Omega}_f$ is readily available if a canonical realization is used for integration of the LPF dynamics. We use \mathbf{a}_f to denote the gravity-corrected LPF acceleration output in the inertial reference frame, *i.e.*,

$$\mathbf{a}_f = \mathbf{R}\mathbf{a}_f^b + g\mathbf{i}_z. \quad (19)$$

A. PD Position and Velocity Control

Position and velocity control is based on two cascaded PD controllers. The cascaded design is convenient from a controller tuning perspective, but mathematically equivalent to the following single expression:

$$\begin{aligned} \mathbf{a}_c &= \mathbf{K}_x (\mathbf{x}_{ref} - \mathbf{x}) + \mathbf{K}_v (\mathbf{v}_{ref} - \mathbf{v}) \\ &\quad + \mathbf{K}_a (\mathbf{a}_{ref} - \mathbf{a}_f) + \mathbf{a}_{ref} \end{aligned} \quad (20)$$

with \mathbf{K}_\bullet indicating diagonal gain matrices.

Throughout this paper, we use the subscript c to indicate commanded values that are computed in one of the control loops. In contrast, the subscript ref indicates a value obtained directly from the reference trajectory, *e.g.*, \mathbf{a}_c includes control terms based on the position and velocity deviations, while \mathbf{a}_{ref} is obtained directly from the reference trajectory as the second derivative of \mathbf{x}_{ref} .

The first three terms in (20) ensure tracking of position and velocity references, while the final term serves as a feedforward input to ensure tracking of the reference acceleration. The control utilizes the inertial reference frame with — in our implementation — identical gains for the horizontal \mathbf{i}_x - and \mathbf{i}_y -directions, but separately tuned gains for the vertical \mathbf{i}_z -direction. The commanded acceleration is used to calculate thrust, roll, and pitch commands, as will be shown in the next section.

B. INDI Linear Acceleration Control

An INDI-based quadcopter linear acceleration controller was derived based on Taylor series approximation in [18]. In this section, we arrive at equivalent control equations using a derivation based on the estimation of the external forces acting on the quadrotor. We find that this derivation helps

intuitive understanding of the practical working of the INDI notion.

By rewriting (2), we obtain an expression for the external force acting on the quadrotor in terms of measured acceleration and specific thrust, as follows:

$$\mathbf{f}_{ext} = m(\mathbf{a}_f - \tau_f \mathbf{b}_z - g\mathbf{i}_z) \quad (21)$$

with τ_f the specific thrust calculated according to (7) using filtered motor speed measurements ω_f . The identical LPF is applied to both IMU measurements and measured motor speeds to ensure that the same phase lag is incurred by both signals [17].

Changes in \mathbf{f}_{ext} are difficult to predict, so we treat it as a constant and substitute its expression (21) into (2):

$$\begin{aligned} \mathbf{a} &= \tau \mathbf{b}_z + g\mathbf{i}_z + m^{-1} \mathbf{f}_{ext} \\ &= \tau \mathbf{b}_z + g\mathbf{i}_z + m^{-1} (m(\mathbf{a}_f - \tau_f \mathbf{b}_z - g\mathbf{i}_z)) \\ &= \tau \mathbf{b}_z - \tau_f \mathbf{b}_z + \mathbf{a}_f. \end{aligned} \quad (22)$$

Even though \mathbf{f}_{ext} is considered as a constant over the IMU measurement interval, fast changes in external force are in practice accounted for by setting the IMU rate sufficiently high.

Based on (22), we compute the specific thrust vector command that results in the commanded acceleration as prescribed by (20), using the following incremental relation:

$$(\tau \mathbf{b}_z)_c = \tau_f \mathbf{b}_z + \mathbf{a}_c - \mathbf{a}_f. \quad (23)$$

The incremental nature of (23) eliminates the need for integral action; if the commanded acceleration is not achieved directly, the thrust and attitude commands will be incremented further in subsequent control updates. Consequently, no integrator gains are needed in (20).

By (6), we have

$$(\tau \mathbf{b}_z)_c = \tau_c \begin{bmatrix} s\psi_{ref}s\phi_c + c\psi_{ref}s\theta_c c\phi_c \\ -c\psi_{ref}s\phi_c + s\psi_{ref}s\theta_c c\phi_c \\ c\theta_c c\phi_c \end{bmatrix}, \quad (24)$$

so that the commanded thrust can directly be obtained as

$$T_c = -m \|(\tau \mathbf{b}_z)_c\|_2 \quad (25)$$

with the negative sign following from the definition that thrust is positive in \mathbf{b}_z -direction. The reference yaw angle ψ_{ref} is prescribed by the reference trajectory, so the commanded roll ϕ_c and pitch θ_c are uniquely defined by (24).

The following expressions — based on trigonometric interpretation of \mathbf{b}_z — are derived in Appendix I:

$$\phi_c = \arcsin\left(\frac{(\tau\mathbf{b}_z)_c^T(\mathbf{i}_x \sin \psi_{ref} - \mathbf{i}_y \cos \psi_{ref})}{\|(\tau\mathbf{b}_z)_c\|_2}\right), \quad (26)$$

$$\theta_c = \arctan\left(\frac{(\tau\mathbf{b}_z)_c^T(\mathbf{i}_x \cos \psi_{ref} + \mathbf{i}_y \sin \psi_{ref})}{(\tau\mathbf{b}_z)_c^T \mathbf{i}_z}\right). \quad (27)$$

C. NDI Attitude and Attitude Rate Control

Inner-loop attitude control is based on NDI. Due to space limitations, the overview in this section consists of key results; the full derivation is given in Appendix II.

Feedback linearization of the angular kinematics allows us to obtain a controller that takes into account nonlinear angular dynamics, but that can be tuned using linear techniques, such as pole placement and LQR [3]. The NDI controller is based on the dynamics system

$$\dot{\chi} = f(\chi) + g(\chi) \dot{\Omega} = \underbrace{\begin{bmatrix} \mathbf{S}\Omega \\ \mathbf{0}_{3 \times 1} \end{bmatrix}}_{f(\chi)} + \underbrace{\begin{bmatrix} \mathbf{0}_{3 \times 3} \\ \mathbf{I} \end{bmatrix}}_{g(\chi)} \dot{\Omega} \quad (28)$$

with $\chi = [\xi^T \ \Omega^T]^T$, and the output function

$$h(\chi) = \xi. \quad (29)$$

The body-frame angular acceleration $\dot{\Omega}$ serves as the input of the state dynamics equation. This has two major advantages compared to using the control torque μ as input. Firstly, the NDI controller does not need to take into account the vehicle inertia matrix \mathbf{J} or any other model-specific parameters. Therefore it does not suffer from inversion discrepancies due to model mismatches. Secondly, the commanded body torque μ is separately determined by the INDI controller described in Section III-D, which considers the external moment μ_{ext} based on IMU measurements. This eliminates the need to incorporate a complicated model of the external moment in (28), and thereby further improves controller robustness and simplicity.

Feedback linearization of (28) results in the following equivalent linear double integrator system:

$$\begin{bmatrix} \dot{\xi} \\ \ddot{\xi} \end{bmatrix} = \begin{bmatrix} \mathbf{0}_{3 \times 3} & \mathbf{I} \\ \mathbf{0}_{3 \times 3} & \mathbf{0}_{3 \times 3} \end{bmatrix} \begin{bmatrix} \xi \\ \dot{\xi} \end{bmatrix} + \begin{bmatrix} \mathbf{0}_{3 \times 3} \\ \mathbf{I} \end{bmatrix} \bar{\mathbf{u}}. \quad (30)$$

The virtual control $\bar{\mathbf{u}}$ is obtained using the NDI control mapping

$$\bar{\mathbf{u}} = L_f^2 h(\chi) + L_g L_f h(\chi) \dot{\Omega} \quad (31)$$

with $L_f^n h(\chi)$ the n -th Lie derivative of the function $h(\chi)$ with regard to the vector field f .

We can now apply linear techniques such as pole placement and LQR to control (30). The controller is designed to track the commanded state $\eta_c = [\xi_c^T \ \dot{\xi}_{ref}^T]^T$. The attitude command $\xi_c = [\phi_c \ \theta_c \ \psi_{ref}]^T$ consists of roll and pitch prescribed by the acceleration controller in (26) and (27), and yaw prescribed directly by the reference trajectory. The first two elements of the attitude rate command $\dot{\xi}_{ref} = [\dot{\phi}_{ref} \ \dot{\theta}_{ref} \ \dot{\psi}_{ref}]^T$ are prescribed by the reference jerk through differential flatness, and the final element is obtained

by differentiation of the reference yaw, as given by (12). The resulting linear controller has the form

$$\mathbf{u} = \mathbf{K}_\xi (\xi_c - \xi) + \mathbf{K}_{\dot{\xi}} (\dot{\xi}_{ref} - \dot{\xi}), \quad (32)$$

where $\dot{\xi}$ has the subscript f because it is obtained by transformation of the filtered gyro rate Ω_f using (3). Note that angular wrapping must be taken into account when subtracting attitude angles in (32).

Through differential flatness, we also obtain the attitude acceleration reference $\ddot{\xi}_{ref} = [\ddot{\phi}_{ref} \ \ddot{\theta}_{ref} \ \ddot{\psi}_{ref}]^T$ as a function of reference snap, and the second derivative of the reference yaw, as given by (16). This attitude acceleration reference is directly added to the virtual control \mathbf{u} to obtain the commanded attitude acceleration:

$$\ddot{\xi}_c = \mathbf{u} + \ddot{\xi}_{ref}. \quad (33)$$

This direct addition of feedback and feedforward control inputs is permitted by linearity of (30). Finally, the commanded angular acceleration in the body-frame $\dot{\Omega}_c$ is obtained by setting $\bar{\mathbf{u}} = \ddot{\xi}_c$ and inverting the NDI control mapping (31), as follows:

$$\begin{aligned} \dot{\Omega}_c &= (L_g L_f h(\chi))^{-1} (\ddot{\xi}_c - L_f^2 h(\chi)) \\ &= \mathbf{S}^{-1} (\ddot{\xi}_c - L_f^2 h(\chi)), \end{aligned} \quad (34)$$

where

$$\begin{aligned} L_f^2 h(\chi) &= \frac{\partial \mathbf{S}\Omega}{\partial \chi} f(\chi) \\ &= \begin{bmatrix} \frac{\partial \mathbf{S}\Omega}{\partial \xi} & \mathbf{S} \end{bmatrix} \begin{bmatrix} \mathbf{S}\Omega \\ \mathbf{0}_{3 \times 1} \end{bmatrix} \\ &= \begin{bmatrix} \frac{s\theta(qc\phi - rs\phi)}{c\theta} & \frac{rc\phi + qs\phi}{c^2\theta} & 0 \\ -rc\phi - qs\phi & 0 & 0 \\ \frac{qc\phi - rs\phi}{c\theta} & \frac{s\theta(rc\phi + qs\phi)}{c^2\theta} & 0 \end{bmatrix} \\ &\quad \begin{bmatrix} p + rc\phi t\theta + qs\phi t\theta \\ qc\phi - rs\phi \\ \frac{rc\phi + qs\phi}{c\theta} \end{bmatrix}. \end{aligned} \quad (35)$$

In practice, (35) is implemented based on Ω_f , but the subscript is not printed here in order to maintain legibility.

The attitude controller differs from a typical nonlinear attitude controller, because it not only tracks the attitude command, but also attitude rate and acceleration based on the trajectory jerk and snap. Essentially, the controller exploits its knowledge of the trajectory to predict future attitude commands. In Section IV, we explore the theoretical implications of these feedforward terms, and in Section V, we experimentally examine how they affect trajectory tracking performance.

D. INDI Angular Acceleration Control

Trajectory tracking based on body rate control, *e.g.*, using an off-the-shelf flight controller, is incapable of considering reference snap, because snap corresponds to the vehicle angular acceleration by (16). Hence, our proposed controller tracks the angular acceleration command $\dot{\Omega}_c$ obtained by

(34). This command incorporates tracking of the reference snap through the feedforward term $\ddot{\xi}_{ref}$.

State-of-the-art INDI control tracks angular acceleration based on linearization of the control effectiveness equation [17], [18]. We present an INDI implementation based on estimation of the external moment μ_{ext} and nonlinear inversion of (7). This results in a nonlinear INDI angular acceleration controller, analogous to the INDI linear acceleration control described in the Section III-B.

We rewrite (4) to obtain the following expression for the external moment based on the measured angular rate, angular acceleration, and control moment:

$$\mu_{ext} = \mathbf{J}\dot{\Omega}_f - \mu_f + \Omega_f \times \mathbf{J}\Omega_f \quad (36)$$

with μ_f the control moment in the body-fixed reference frame, obtained from the measured motor speed ω_f by (7).

Analogous to the external force in Section III-B, the external moment μ_{ext} is considered a constant, because its behavior is unmodeled. Substitution of (36) into (4) then gives:

$$\begin{aligned} \dot{\Omega} &= \mathbf{J}^{-1}(\mu + \mu_{ext} - \Omega \times \mathbf{J}\Omega) \\ &= \mathbf{J}^{-1}(\mu + (\mathbf{J}\dot{\Omega}_f - \mu_f + \Omega_f \times \mathbf{J}\Omega_f) - \Omega \times \mathbf{J}\Omega) \\ &= \dot{\Omega}_f + \mathbf{J}^{-1}(\mu - \mu_f). \end{aligned} \quad (37)$$

The change in the contribution of angular momentum is neglected under the assumption of separation of time scales; it is assumed to be much slower changing compared to the motor dynamics. By inversion of the final line of (37), we obtain the control moment command required to achieve the commanded angular acceleration $\dot{\Omega}_c$, as follows:

$$\mu_c = \mu_f + \mathbf{J}(\dot{\Omega}_c - \dot{\Omega}_f). \quad (38)$$

E. Inversion-Based Moment and Thrust Control, and Integrative Motor Speed Control

So far, we have computed the commanded thrust T_c and control moment μ_c by (25) and (38), respectively. Tracking of these commands requires control of the motor speeds as can be observed from the direct relation given in (7). Fast and accurate motor speed control can be achieved using loop closure based on motor speed feedback. Moreover, accurate motor speed measurements are also required in INDI control for calculation of τ_f and μ_f in (23) and (38), respectively. To obtain the motor speeds, we employ an optical encoder that measures the motor rotation period by detecting the passage of a reflective strip on the side of the motor hub. The optical encoder, shown in Fig. 5, provides a high-rate, accurate, lightweight and unintrusive manner to obtain the motor speed.

The commanded thrust and control moment are used to solve (7) for the commanded motor speeds. In order to do so, the equation is discretized using finite-difference approximation over the time interval Δt , resulting in the following relation:

$$\begin{bmatrix} \mu_c \\ T_c \end{bmatrix} = \mathbf{G}_1 \omega_c^{\circ 2} + \Delta t^{-1} \mathbf{G}_2 (\omega_c - \omega_f), \quad (39)$$



Fig. 5: Motor (propeller removed) with optical encoder that measures rotation speed. The optical encoder lens, and accompanying reflective strip can be seen to the right, and on the front side of the motor hub, respectively.

which can be solved numerically to obtain the commanded motor speed vector ω_c , *e.g.*, using Newton's method. Inversion of this nonlinear control effectiveness relation improves the accuracy of thrust and control moment tracking, when compared to the linearized inversion as shown in [18] (see also (80)).

The pulse width modulation vector ζ contains the commands that are sent to the four ESCs, and is obtained as follows:

$$\zeta = p(\omega_c) + \mathbf{K}_{I\omega} \int \omega_c - \omega dt \quad (40)$$

with p a vector-valued polynomial function relating motor speeds to PWM inputs. This function was obtained by regression analysis of static test data. Integral action is added to account for loss of control effectiveness with decreasing battery voltage. The measured signal ω remains unfiltered here to minimize phase lag.

IV. RESPONSE ANALYSIS

The application of incremental control and the tracking of high-order derivatives of the reference trajectory are key aspects of our control design. In this section, we establish the advantages of these features by analyzing the tracking and disturbance rejection characteristics of the closed-loop quadrotor system. We verify the improved robustness of incremental NDI against disturbances and modeling errors by comparing it to nonincremental, *i.e.*, regular, NDI. Furthermore, we show how the feedforward terms based on higher-order derivatives of the trajectory reference, *i.e.*, jerk and snap, improve the tracking of a fast-changing acceleration signal. In order to analyze the behavior of the closed-loop dynamics, we use linearized dynamics and control equations in this section. Our findings are validated using real-life flights in Section V.

A. Linearized Dynamics

We analyze the acceleration and position tracking response in the forward, *i.e.*, \mathbf{i}_x , direction. The dynamics in

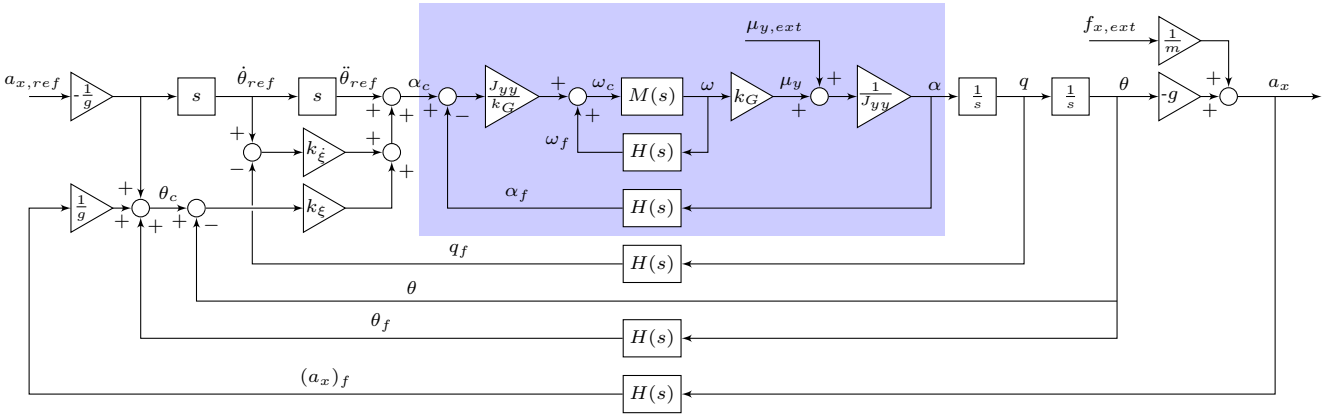


Fig. 6: Linearized closed-loop forward acceleration dynamics, with pitch acceleration dynamics in blue area.

the Laplace domain are obtained by linearizing the system around the hover state. We isolate the pitch and forward acceleration dimensions in (2) and (4) to obtain

$$a_x = \tau \sin \theta + m^{-1} f_{x,ext}, \quad (41)$$

$$J_{yy} \dot{q} = \mu_y + \mu_{y,ext}, \quad (42)$$

where J_{yy} is the vehicle moment of inertia about the \mathbf{b}_y -axis. Given the symmetries of the quadrotor, only elements on the diagonal of the inertia tensor \mathbf{J} are nonzero. We use the subscript x to indicate a forward component, e.g., $a_{x,ref} = \mathbf{a}_{ref}^T \mathbf{i}_x$, and the subscript y to indicate a pitch component, e.g., $\mu_y = \boldsymbol{\mu}^T \mathbf{i}_y$. In hover condition, we have $\tau = -g$, $\theta = 0$, and $p = q = r = 0$, so that (41) and (42) can be linearized to obtain

$$a_x = -g\theta + m^{-1} f_{x,ext}, \quad (43)$$

$$J_{yy} \dot{q} = \mu_y + \mu_{y,ext}. \quad (44)$$

B. Linearized Control Laws

We isolate the forward acceleration component in the incremental INDI linear acceleration control law (23) to obtain

$$\tau_c \sin \theta_c = \tau_f \sin \theta + a_{x,ref} - a_{x,f}. \quad (45)$$

The filtered acceleration \mathbf{a}_f in (23) is obtained by (19). Substitution of this expression in (45) gives

$$\begin{aligned} \tau_c \sin \theta_c &= \tau_f \sin \theta + a_{x,ref} \\ &\quad - (a_x \cos \theta - (a_z - g) \sin \theta)_f \cos \theta \\ &\quad - (a_x \sin \theta + (a_z - g) \cos \theta)_f \sin \theta. \end{aligned} \quad (46)$$

We linearize around the hover condition, and obtain

$$-g\theta_c = a_{x,ref} - (a_x)_f - g\theta_f \quad (47)$$

with $(a_x)_f$ the filtered forward acceleration a_x . Rewriting (47) gives the following expression for the commanded pitch angle:

$$\theta_c = \theta_f - \frac{a_{x,ref}}{g} + \frac{(a_x)_f}{g}. \quad (48)$$

In standard hover condition, the body and inertial reference systems coincide and angular rates are zero, so that the

NDI state and control mappings described in Section III-C reduce to the identity map. Therefore the commanded pitch acceleration is obtained by taking the pitch component of (32) and (33), as follows:

$$\dot{q}_c = k_\xi (\theta_c - \theta) + k_{\dot{\xi}} (\dot{\theta}_{ref} - q_f) + \ddot{\theta}_{ref}. \quad (49)$$

The scalar control gains k_ξ and $k_{\dot{\xi}}$ are obtained by selecting the pitch elements from the corresponding control gain matrices described in Section III. By linearization of (12) and (16), we have $\dot{\theta}_{ref} = -\frac{j_{x,ref}}{g}$ and $\ddot{\theta}_{ref} = -\frac{s_{x,ref}}{g}$. Substitution into (49) gives the following expression for the commanded angular acceleration:

$$\dot{q}_c = k_\xi (\theta_c - \theta) + k_{\dot{\xi}} \left(-\frac{j_{x,ref}}{g} - q_f \right) - \frac{s_{x,ref}}{g}, \quad (50)$$

where $j_{x,ref}$ and $s_{x,ref}$ are the reference jerk and snap, respectively.

Next, we linearize the angular acceleration and moment control laws. For convenience of expression, we model the four motors collectively. This method is valid, as the system is linearized around the hover state where all motors have identical angular speeds. The scalar value ω (with its various subscripts) refers to the deviation from the hover state motor speed ω_0 , or equivalently to half of the angular speed difference between the front and rear motors. Equating (38) and (39), and isolating the pitch channel gives

$$4l_x k_\tau (\omega_0 + \omega_c)^2 = 4l_x k_\tau (\omega_0 + \omega_f)^2 + J_{yy}(\dot{q}_c - \dot{q}_f) \quad (51)$$

with the factor 4 due to the number of motors. Rewriting (51) gives the following expression for the commanded motor speed:

$$\omega_c = \sqrt{(\omega_0 + \omega_f)^2 + J_{yy}(4l_x k_\tau)^{-1}(\dot{q}_c - \dot{q}_f)} - \omega_0. \quad (52)$$

Linearization around the hover state gives

$$\omega_c = \omega_f + J_{yy} k_G^{-1}(\dot{q}_c - \dot{q}_f), \quad (53)$$

with the linearized control effectiveness gain $k_G = 8\omega_0 l_x k_\tau$, so that

$$\mu_y = k_G \omega. \quad (54)$$

C. Closed-Loop Transfer Functions

We have obtained linearized dynamics and control laws for forward acceleration and pitch. Next, we will combine the linearized equations to obtain the transfer functions that describe the acceleration dynamics in the Laplace domain. For this purpose, we denote the LPF transfer function by $H(s)$, so that for example $\frac{\omega_f}{\omega}(s) = H(s)$, and we denote the motor control and dynamics by $M(s)$, so that $\frac{\omega_c}{\omega_c}(s) = M(s)$.

By combining (44), (53), and (54), we obtain the linearized closed-loop pitch acceleration dynamics shown in the blue area in Fig. 6 and represented by the transfer functions

$$\frac{\alpha}{\alpha_c}(s) = \frac{J_{yy}k_G^{-1} \frac{M(s)}{1-M(s)H(s)} k_G J_{yy}^{-1}}{1 + J_{yy}k_G^{-1} \frac{M(s)}{1-M(s)H(s)} k_G J_{yy}^{-1} H(s)} = M(s), \quad (55)$$

$$\frac{\alpha}{\mu_{y,ext}}(s) = \frac{J_{yy}^{-1}}{1 + \frac{H(s)M(s)}{1-H(s)M(s)}} = J_{yy}^{-1} (1 - H(s)M(s)) \quad (56)$$

with $\alpha(s)$ the pitch acceleration, *i.e.*, $\alpha(s) = sq(s) = s^2\theta(s)$. We observe that the closed-loop angular acceleration dynamics are solely determined by the motor dynamics. This result was previously obtained for linearized INDI angular acceleration control in [17]. The disturbance moment $\mu_{y,ext}$ is immediately corrected for as it propagates through the angular acceleration feedback loop and motor dynamics. This is done incrementally by comparing the expected angular acceleration from the motor speeds, *i.e.*, $\frac{k_G}{J_{yy}}\omega$, to the measured angular acceleration, *i.e.*, α_f , which includes the effects of the disturbance moment. The low-frequency gain of (56) is zero, so that the disturbance is damped within the angular acceleration controller without any steady-state error.

We can now combine (43), (49), (50), (55), and (56) to obtain the linearized forward acceleration dynamics as shown in Fig. 6 and represented by the transfer functions

$$\frac{a_x}{a_{x,ref}}(s) = \frac{M(s)(s^2 + k_\xi s + k_\xi)}{s^2 + k_\xi H(s)M(s)s + k_\xi M(s)}, \quad (57)$$

$$\frac{a_x}{f_{x,ext}}(s) = \frac{1}{m} - \frac{1}{m} \frac{H(s)M(s)k_\xi}{s^2 + k_\xi H(s)M(s)s + k_\xi M(s)}, \quad (58)$$

$$\frac{a_x}{\mu_{y,ext}}(s) = \frac{g}{J_{yy}} \frac{H(s)M(s) - 1}{s^2 + k_\xi H(s)M(s)s + k_\xi M(s)}. \quad (59)$$

Similar to the moment, the disturbance force $f_{x,ext}$ is corrected for within the acceleration controller. This is done incrementally using the difference of the acceleration due to thrust, *i.e.*, $-g\theta_f$, and the true acceleration including the disturbance force, *i.e.*, $(a_x)_f$. Consequently, also (58) has zero steady-state gain.

In order to evaluate the effect of the disturbance force and moment on the position tracking error, we close the loop around (58) and (59) using the linear PD position and velocity control given in (20). We denote the resulting transfer functions $\frac{x}{f_{x,ext}}(s)$ and $\frac{x}{\mu_{y,ext}}(s)$, but do not show their copious expressions here.

D. Robustness against Disturbance Forces and Moments

In order to demonstrate the disturbance rejection capability of INDI, we compare the proposed controller to a nonincremental controller, *e.g.*, a regular NDI controller.

The nonincremental linear acceleration control law is given by (cf. (45))

$$\tau_c \sin \theta_c = a_{x,ref}, \quad (60)$$

which is linearized to obtain (cf. (48))

$$\theta_c = -\frac{a_{x,ref}}{g}. \quad (61)$$

We use the following relation for angular acceleration control (cf. (51)):

$$4l_x k_\tau (\omega_0 + \omega_c)^2 = J_{yy} \dot{q}_c \quad (62)$$

with \dot{q}_c still given by (50). Linearization gives (cf. (53))

$$\omega_c = \frac{J_{yy}}{k_G} \dot{q}_c. \quad (63)$$

This nonincremental controller has the same angular acceleration tracking response as the proposed incremental control design, *i.e.*,

$$\frac{\alpha}{\alpha_{c NI}}(s) = \frac{\alpha}{\alpha_c}(s) = M(s) \quad (64)$$

with the subscript *NI* indicating that the transfer function corresponds to the nonincremental controller. However, due to the lack of incremental control, the α_f and ω_f feedback loops disappear, so that (cf. (56))

$$\frac{\alpha}{\mu_{y,ext NI}}(s) = J_{yy}^{-1}. \quad (65)$$

The disturbance moment now propagates undamped to the attitude and position control loops, as there is no closed-loop angular acceleration control that directly evaluates the moments acting on the vehicle.

Like the angular acceleration tracking response, the linear acceleration tracking response is identical to the one for the proposed incremental control design, *i.e.*,

$$\frac{a_x}{a_{x,ref NI}}(s) = \frac{a_x}{a_{x,ref}}(s). \quad (66)$$

On the other hand, the disturbance responses are quite different in the case of nonincremental control, and given by

$$\frac{a_x}{f_{x,ext NI}}(s) = \frac{1}{m}, \quad (67)$$

$$\frac{a_x}{\mu_{y,ext NI}}(s) = \frac{g}{J_{yy}} \frac{-1}{s^2 + k_\xi H(s)M(s)s + k_\xi M(s)}. \quad (68)$$

It can be seen that the disturbance force $f_{x,ext}$ is now only counteracted in the position and velocity control loops, and while the disturbance moment $\mu_{y,ext}$ is counteracted by the attitude controller, a steady-state acceleration error persists as

$$\lim_{s \rightarrow 0} \frac{a_x}{\mu_{y,ext NI}}(s) = -\frac{g}{J_{yy}k_\xi}. \quad (69)$$

From transfer functions presented above, it can be concluded that the incremental NDI controller has identical reference

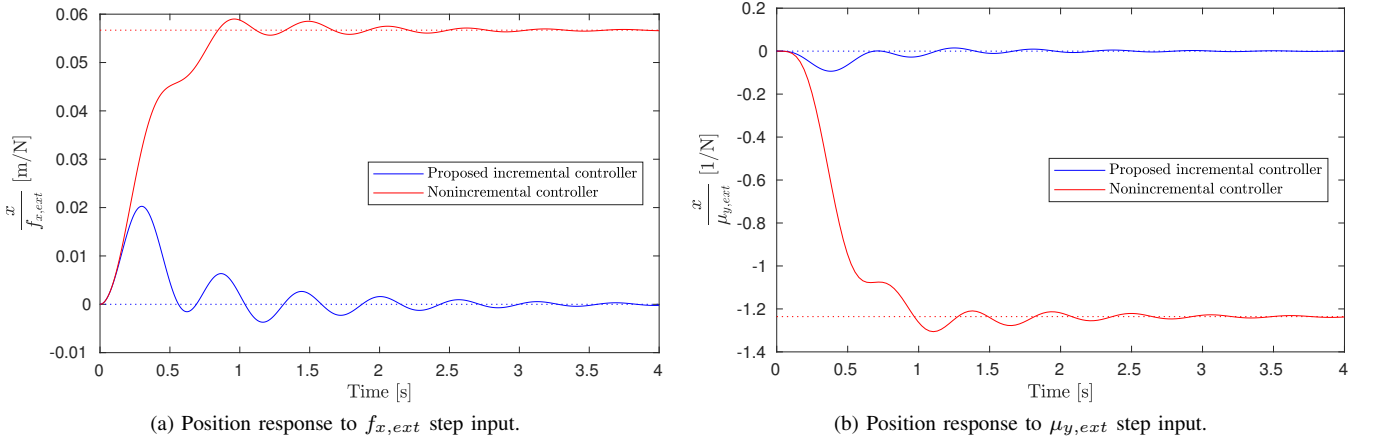


Fig. 7: Simulated disturbance response using the proposed incremental controller, and a nonincremental controller.

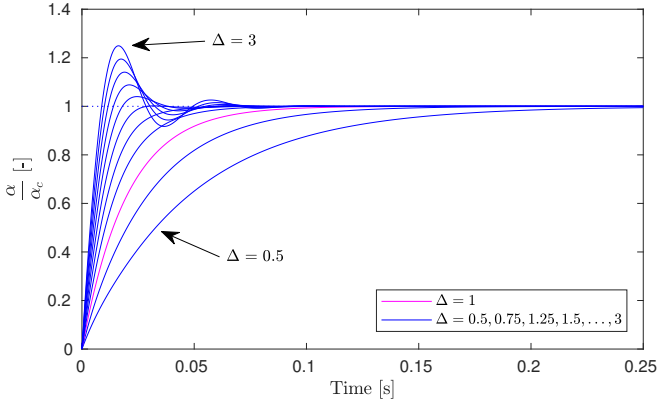


Fig. 8: Simulated angular acceleration step response for various modeling errors using the proposed incremental controller.

tracking performance, but superior disturbance rejection performance when compared to the nonincremental NDI controller.

We close the PD position and velocity control loop and obtain $\frac{x}{f_{x,ext} NI}(s)$ and $\frac{x}{\mu_{y,ext} NI}(s)$ based on the nonincremental controller. Figure 7 shows the step response for these transfer functions along with their counterparts for the proposed incremental control design. The response was simulated using the control gains given in Table III, a second-order Butterworth filter with cutoff frequency equal to 188.5 rad/s (30 Hz), and the following first-order motor model:

$$M(s) = \frac{1}{\tau_m s - 1} \quad (70)$$

with τ_m set to 20 ms. It can be seen that the proposed incremental controller is able to counteract the disturbances and reaches zero steady-state error, while the nonincremental controller is unable to do so.

In order to null the steady-state errors due to force and moment disturbances, integral action must be added to the nonincremental controller. This is not necessary in the case of INDI, so that our proposed control design is able to

quickly and wholly counteract disturbance forces and moments, while avoiding the negative effects that integral action typically has on the tracking performance, *e.g.*, increased overshoot and settling time, and degraded stability.

E. Robustness against Modeling Errors

The proposed control design takes into account several vehicle parameters, namely the mass m , the moment of inertia tensor \mathbf{J} , and the control effectiveness matrices \mathbf{G}_1 and \mathbf{G}_2 . Accurately measuring the moment of inertia and the control effectiveness can be challenging, so it is desirable that tracking performance is maintained if erroneous parameters are used.

The linearized control equations described above incorporate the ratio of the moment of inertia J_{yy} and the linearized control effectiveness k_G . We denote the values used in the controller \bar{J}_{yy} and \bar{k}_G , and define the modeling error Δ such that

$$\frac{\bar{J}_{yy}}{\bar{k}_G} = \Delta \frac{J_{yy}}{k_G}. \quad (71)$$

This leads to the following pitch acceleration dynamics for the proposed incremental NDI controller, and the nonincremental controller described above:

$$\frac{\alpha}{\alpha_c}(s) = \frac{\Delta M(s)}{(\Delta - 1)H(s)M(s) + 1}, \quad (72)$$

$$\frac{\alpha}{\alpha_{cNI}}(s) = \Delta M(s). \quad (73)$$

It can be seen that the error acts as a simple gain in the nonincremental controller, leading to an incorrect angular acceleration. On the contrary, the proposed incremental controller compares the expected angular acceleration from the motor speeds, *i.e.*, $\frac{k_G}{J_{yy}}\omega$, to the measured angular acceleration, *i.e.*, α_f , to correct for the modeling error. The corresponding angular acceleration responses for several values of Δ are shown in Fig. 8. The figure shows that the modeling error affects the transient response, but that the incremental controller is able to correct for it and reaches the commanded acceleration value in all cases.

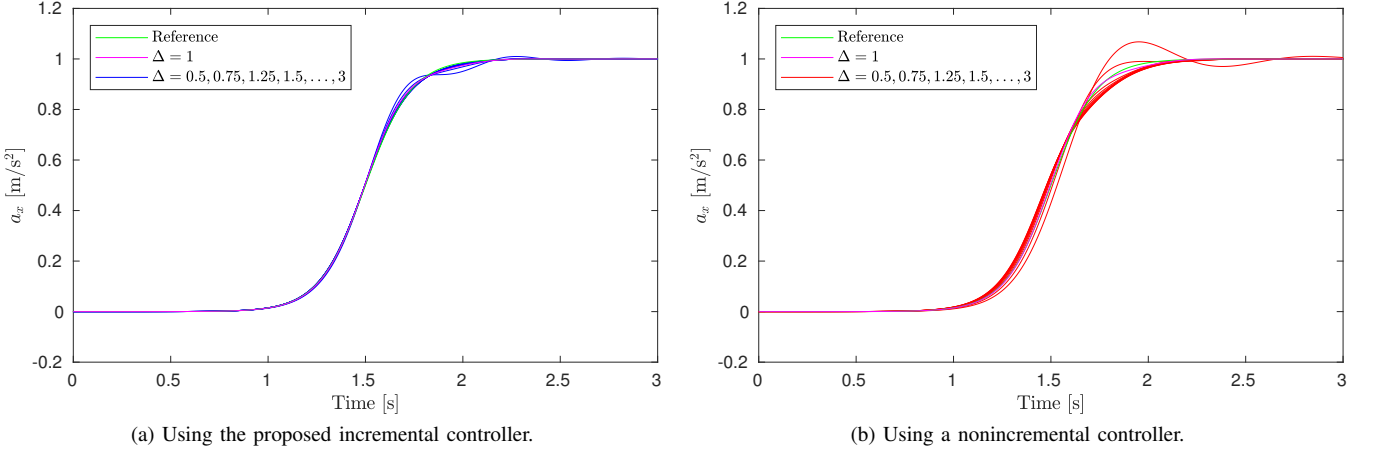


Fig. 9: Simulated linear acceleration tracking response for various modeling errors.

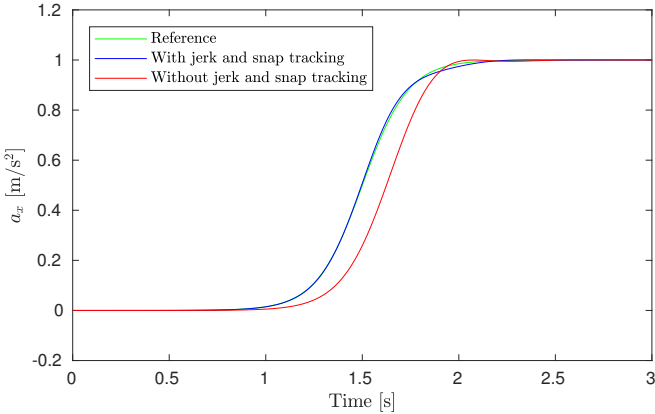


Fig. 10: Simulated linear acceleration tracking response using the proposed controller with and without jerk and snap tracking.

Adding the linear acceleration control law to (72) and (73) results in the following forward acceleration dynamics:

$$\begin{aligned} \frac{a_x}{a_{x,ref}}(s) &= \\ &\frac{\Delta M(s) (s^2 + k_\xi s + k_\xi)}{((\Delta - 1)H(s)M(s) + 1)s^2 + \Delta k_\xi H(s)M(s)s + \Delta k_\xi M(s)}, \\ \frac{a_x}{a_{x,ref NI}}(s) &= \frac{\Delta M(s) (s^2 + k_\xi s + k_\xi)}{s^2 + \Delta k_\xi H(s)M(s)s + \Delta k_\xi M(s)}. \end{aligned} \quad (74)$$

In order to assess the effect of modeling errors on forward acceleration tracking, we simulate the time response of these transfer functions to the following reference signal:

$$a_{x,ref}(t) = \frac{1}{2} \tanh\left(\frac{4}{3}\pi t - 2\pi\right) + \frac{1}{2}. \quad (76)$$

The reference signal is C^2 , i.e., the corresponding jerk and snap signals are continuous, and has boundary conditions $a_{x,ref}(0) = j_{x,ref}(0) = s_{x,ref}(0) = j_{x,ref}(3) =$

$s_{x,ref}(3) = 0$ and $a_{x,ref}(0) = 1$. The responses for various values of Δ are shown in Fig. 9. It can be seen that the incremental controller is able to accurately track the reference signal even when large modeling errors are present. When the nonincremental is used, the tracking performance declines more severely with growing modeling error.

F. Jerk and Snap Tracking

Jerk and snap tracking is a key attribute of the proposed controller design. The tracking of these acceleration derivatives is visible in (57) through the terms $k_\xi s$ and s^2 in the nominator. Without these terms the closed-loop acceleration tracking dynamics reduce to

$$\frac{a_x}{a_{x,ref}}(s) = \frac{M(s)k_\xi}{s^2 + k_\xi H(s)M(s)s + k_\xi M(s)}. \quad (77)$$

Comparison of (57) and (77) shows that the feedforward terms add two zeros to the closed-loop transfer function. These zeros — in combination with the LPF — act essentially as a lead compensator and help improve the transient response of the system. Effective placement of the zeros through tuning of k_ξ leads to improved tracking of a rapidly changing acceleration input signal, e.g., during aggressive flight maneuvers. Conveniently, the gain k_ξ can be tuned using linear control techniques, as described in Section III-C.

Figure 10 shows the simulated response of (57) and (77) to the reference signal defined in (76). It can be seen that the inclusion of jerk and snap tracking causes a faster response and decrease in overshoot, resulting in more accurate acceleration tracking. In the next section, we show that the same improvements are achieved in practice.

V. EXPERIMENTAL RESULTS

In this section, experimental results for high-speed, high-acceleration flight are presented. A video of the experiments is available at <https://youtu.be/M11E9M1FmVA>. We evaluate the performance of the trajectory tracking controller on two trajectories: A complicated 3D trajectory that includes

TABLE III: Trajectory tracking controller gains.

| Gain | Value |
|--------------------------|----------------------|
| \mathbf{K}_x | diag ([18 18 13.5]) |
| \mathbf{K}_v | diag ([7.8 7.8 5.9]) |
| \mathbf{K}_a | diag ([0.5 0.5 0.3]) |
| \mathbf{K}_ξ | diag ([90 90 16.5]) |
| $\mathbf{K}_{\dot{\xi}}$ | diag ([10 10 14]) |

yawing, tight turns with acceleration up to 2 g, and high-speed straights at up to 8.2 m/s; and a 3D lemniscate trajectory that includes aggressive accelerations at the corners and a top speed of 6.9 m/s. Furthermore, we examine the effect of the feedforward inputs based on the reference trajectory jerk and snap. We establish the controller's independence of any model-based drag estimate by attaching a drag-inducing cardboard plate that more than doubles the frontal area of the vehicle. Robustness against external disturbance forces is further displayed by pulling on a string attached to the quadcopter in hover. Finally, we compare the proposed nonlinear INDI angular acceleration control to its linearized counterpart.

A. Experimental Setup

Experiments were performed in an indoor flight room using the quadcopter shown in Fig. 1. The quadrotor body is 3D-printed using Markforged Onyx. Adjacent motors are mounted 18 cm apart. DJI Snail ESCs and motors are used with the 5048S Tri-Blade racing propeller. Control computations are performed at 500 Hz using an onboard Nvidia Jetson TX2 system-on-module. The quadcopter is powered by a single 4S LiPo battery. The total flying mass is 980 g.

Linear acceleration and angular rate measurements are obtained from an onboard Xsens MTi-3 IMU at 100 Hz, while position, velocity, and orientation measurements are obtained from an OptiTrack motion capture system at 360 Hz with an average latency of 12 ms. The latency is corrected for by propagating motion capture data using integrated IMU measurements. Optical encoders are attached to the motors to measure the motor speeds at 400 Hz. Low-pass filtering of IMU and motor speed measurements is performed using a software second-order Butterworth filter with cutoff frequency 188.5 rad/s (30 Hz).

The controller requires few platform-specific parameters. Exceptions are the vehicle mass m , moment of inertia \mathbf{J} , control effectivenesses matrices \mathbf{G}_1 and \mathbf{G}_2 , and the gain and polynomial fit used by the motor speed controller. In this case, the control effectiveness data were obtained by static tests using the measurement set-up described in [46]. Table III gives an overview of the remaining control gains. Theoretically, the gains listed in this table are platform-independent and usable across different quadrotors without the need for extensive retuning. In practice, we have observed that some retuning is still beneficial for controller performance, when migrating to a platform with a different propulsion system or distinct dynamical characteristics.

B. Evaluation of Proposed Controller

In this section, we evaluate the performance of the trajectory tracking controller on two trajectories: a complicated 3D trajectory, and a lemniscate-shaped trajectory. The former is defined as follows:

$$\boldsymbol{\sigma}_{ref}(t) = \begin{bmatrix} r_{xy} (\sin kt + \cos kt - \cos 2kt) \\ r_{xy} (\cos kt - \cos 2kt + \cos \frac{2}{3}kt - 1) \\ r_z (\cos 2kt + \sin kt - 1) \\ \dot{\psi}_{ref} t \end{bmatrix} \quad (78)$$

with $r_{xy} = 1.5$ m, $r_z = 0.5$ m, and k a parameter used to set velocity. The reference yaw rate $\dot{\psi}_{ref}$ is constant. Figure 11 shows the reference trajectory, along with experimental results for various k and ψ_{ref} . Corresponding performance data are given in Table IV. Each positional reference lap is traversed in $\frac{6\pi}{k}$ s, but the yaw angle reference signal is not synchronized between these laps.

The experiment with $k = 1.125$ rad/s reaches a maximum speed of 8.2 m/s, while maintaining an RMS position tracking error of 4.0 cm. The position error components and Euclidean norm are shown in respectively Fig. 12a and Fig. 12c, and the trajectory speed is shown in Fig. 13. The vehicle attains a maximum acceleration of 19 m/s² (2 g).

To demonstrate trajectory tracking performance in flight with high commanded yaw rate, three flights are performed with $k = 0.9$ rad/s, and $\psi_{ref} = 0$ rad/s, $\psi_{ref} = \frac{\pi}{2}$ rad/s and $\psi_{ref} = \pi$ rad/s, respectively. The resulting position error is shown in Fig. 12b and Fig. 12d. It can be seen that the trajectory tracking controller is able to maintain accurate tracking of the position reference, even if a high yaw rate is prescribed. An RMS position tracking error of no more than 2.0 cm is achieved for $\dot{\psi}_{ref} = 0$ rad/s and $\dot{\psi}_{ref} = \frac{\pi}{2}$ rad/s. For $\dot{\psi}_{ref} = \pi$ rad/s, the error increases somewhat to 2.8 cm. Figure 14 shows that consistent yaw reference tracking performance is achieved even for large yaw rates.

The second, lemniscate-shaped, trajectory is defined as

$$\boldsymbol{\sigma}_{ref}(t) = \begin{bmatrix} r_{xy} \sin 2kt \\ -r_{xy} \cos kt \\ r_z (1 - \cos 2kt) + r_{z_0} \\ 0 \end{bmatrix} \quad (79)$$

with $r_{xy} = 3.14$ m, $r_z = 0.5$ m, $k = 0.95$ rad/s, and r_{z_0} a constant offset. The trajectory, shown in Fig. 15, is a three-dimensional lemniscate, as the sides are flown 1 m higher than the center. The trajectory is challenging as it includes high speed on the diagonal straights and large accelerations for the aggressive turns at the corners. Each identical lap is traversed in $\frac{2\pi}{k}$ s.

The position tracking error is shown in blue in Fig. 16, and tracking performance metrics are given in the first column of Table V. Comparison of the position tracking error to the values in Table IV confirms that the controller achieves consistent performance across trajectories. While the lemniscate trajectory is challenging to fly at high speed and high acceleration, its geometry is relatively simple. This eases interpretation of experimental results. Therefore, we use the trajectory defined by (79) to examine several

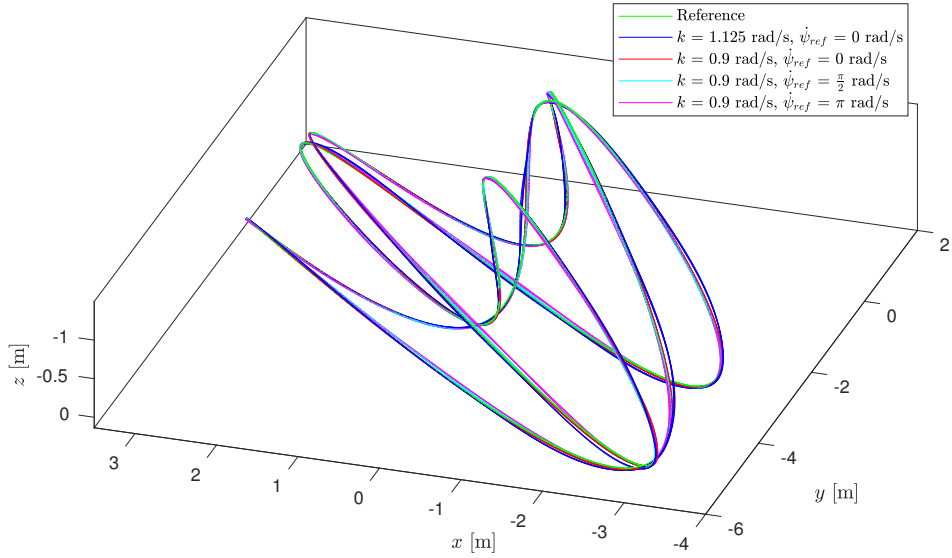


Fig. 11: 3D trajectory for experiments with various reference trajectory parameters.

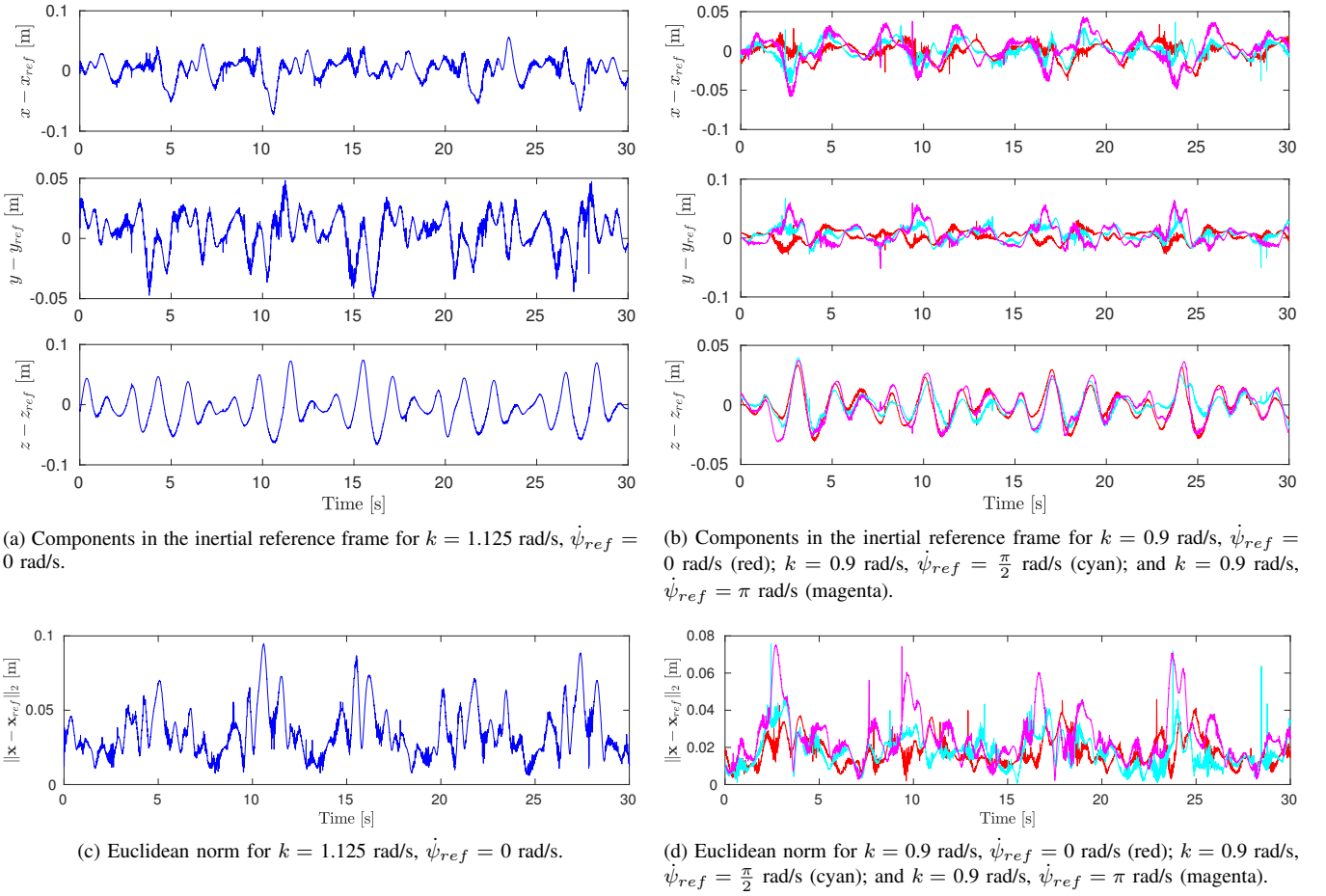


Fig. 12: 3D trajectory position tracking error.

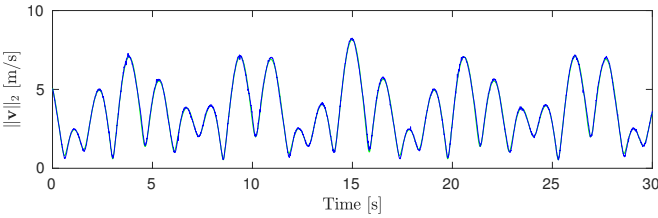


Fig. 13: 3D trajectory Euclidean norm of velocity for reference trajectory (green) and experiment (blue) with $k = 1.125$ rad/s, $\dot{\psi}_{ref} = 0$ rad/s.

modifications to the control design in subsequent sections. In all cases, the trajectory parameters are identical to those used here.

C. Jerk and Snap Tracking

The red curves in Fig. 15 and Fig. 16 correspond to our proposed control design, but with jerk and snap tracking disabled, *i.e.*, $\dot{\xi}_{ref} = \ddot{\xi}_{ref} = \mathbf{0}_{3 \times 1}$. Examination of the figures shows the significant improvement in trajectory tracking performance obtained through the tracking of the jerk and snap feedforward terms. This observation is confirmed by comparing the first two columns of Table V. It can be seen that the root-mean-squared (RMS) position tracking error increases from 3.9 cm to 10.2 cm when jerk and snap tracking are disabled. In Section IV, it was shown that lead compensation provided by jerk and snap tracking results in improved performance when tracking fast-changing acceleration commands. This effect can also be observed in Fig. 17, which shows the vehicle speed and acceleration. It can be seen that the system response has less overshoot when jerk and snap tracking are enabled, conform the analytical response of the linearized system.

D. Increased Aerodynamic Drag

The magenta curves in Fig. 15 and Fig. 16 correspond to the trajectory tracking controller as described in this paper, but using the quadcopter with attached drag plate. The drag plate is a 10 cm \times 30 cm cardboard plate that is attached to the bottom of the quadrotor, as shown in Fig. 18. The plate more than doubles the frontal surface area of the quadrotor, and as such has a significant effect on the aerodynamic force and moment that act on the vehicle,

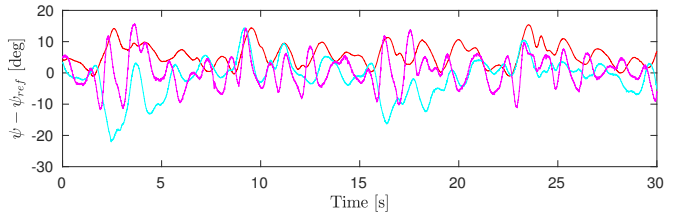


Fig. 14: 3D trajectory yaw error for experiments with $k = 0.9$ rad/s, $\dot{\psi}_{ref} = 0$ rad/s (red); $k = 0.9$ rad/s, $\dot{\psi}_{ref} = \frac{\pi}{2}$ rad/s (cyan); and $k = 0.9$ rad/s and $\dot{\psi}_{ref} = \pi$ rad/s (magenta).

especially during high-speed flight, and fast pitch and yaw motion. The flight controller is not adapted in any way to account for either these aerodynamic effects, or the changes in mass and moment of inertia.

Comparison of columns (i) and (iii) in Table V shows that the loss of performance due to the drag plate is small. This demonstrates the robustness property of INDI. Controllers that depend on the estimation of drag forces based on velocity, such as [26] and [40], may suffer from much larger loss of tracking performance when the aerodynamic properties of the vehicle are modified. Instead of depending on a model-based drag estimate, INDI counteracts the disturbance force and moment by sensor-based incremental control.

The controller implicitly estimates the external force by (21). In Fig. 19, it can be seen that the drag plate has a significant effect on the external disturbance force: its estimated magnitude increases by approximately 50%. In order to counteract the greater external force, thrust and vehicle pitch increase when the drag spoiler is attached.

E. Nonlinear INDI Angular Acceleration Control

The final column of Table V lists data for the trajectory tracking controller as described in this paper, but using linearized INDI angular acceleration control as presented in [18]. Control moment and thrust are tracked using linearized inversion of (7), as follows:

$$\boldsymbol{\omega}_c = \boldsymbol{\omega}_f + (2\mathbf{G}_1 + \Delta t^{-1}\mathbf{G}_2) \left(\begin{bmatrix} \boldsymbol{\mu}_c - \boldsymbol{\mu}_f \\ T_c - T_f \end{bmatrix} + \Delta t^{-1}\mathbf{G}_2 B(\boldsymbol{\omega}_c - \boldsymbol{\omega}_f) \right), \quad (80)$$

where B is the one-sample backshift operator. This inversion does not take into account local nonlinearity of (7).

TABLE IV: 3D trajectory tracking performance for experiments with various reference trajectory parameters.

| k [rad/s] | 1.125 | 0.9 | 0.9 | 0.9 |
|---|-------|-----|-----------------|-------|
| $\dot{\psi}_{ref}$ [rad/s] | 0 | 0 | $\frac{\pi}{2}$ | π |
| RMS $\ \mathbf{x} - \mathbf{x}_{ref}\ _2$ [cm] | 4.0 | 1.8 | 2.0 | 2.8 |
| max $\ \mathbf{x} - \mathbf{x}_{ref}\ _2$ [cm] | 9.4 | 4.1 | 4.8 | 6.5 |
| RMS $ \psi - \psi_{ref} $ [deg] | 15 | 6.7 | 6.7 | 5.0 |
| max $ \psi - \psi_{ref} $ [deg] | 36 | 14 | 21 | 16 |
| RMS $\ \mathbf{v}\ _2$ [m/s] | 4.2 | 3.3 | 3.3 | 3.3 |
| max $\ \mathbf{v}\ _2$ [m/s] | 8.2 | 6.6 | 6.6 | 6.6 |
| RMS $\ \mathbf{a} - \mathbf{g}\ _2$ [m/s ²] | 13 | 11 | 11 | 11 |
| max $\ \mathbf{a} - \mathbf{g}\ _2$ [m/s ²] | 19 | 15 | 15 | 15 |

TABLE V: Lemniscate trajectory tracking performance for: (i) the trajectory tracking controller as proposed in this paper; (ii) jerk and snap tracking disabled; (iii) drag plate attached; and (iv) linearized angular acceleration INDI control.

| | (i) | (ii) | (iii) | (iv) |
|---|-----|------|-------|------|
| RMS $\ \mathbf{x} - \mathbf{x}_{ref}\ _2$ [cm] | 3.9 | 10.2 | 4.5 | 4.1 |
| max $\ \mathbf{x} - \mathbf{x}_{ref}\ _2$ [cm] | 7.6 | 15.8 | 7.9 | 7.6 |
| RMS ψ [deg] | 11 | 11 | 12 | 14 |
| max $ \psi $ [deg] | 25 | 26 | 21 | 26 |
| RMS $\ \mathbf{v}\ _2$ [m/s] | 4.8 | 4.9 | 4.9 | 4.8 |
| max $\ \mathbf{v}\ _2$ [m/s] | 6.9 | 7.0 | 6.8 | 6.8 |
| RMS $\ \mathbf{a} - \mathbf{g}\ _2$ [m/s ²] | 13 | 13 | 13 | 13 |
| max $\ \mathbf{a} - \mathbf{g}\ _2$ [m/s ²] | 16 | 16 | 16 | 16 |

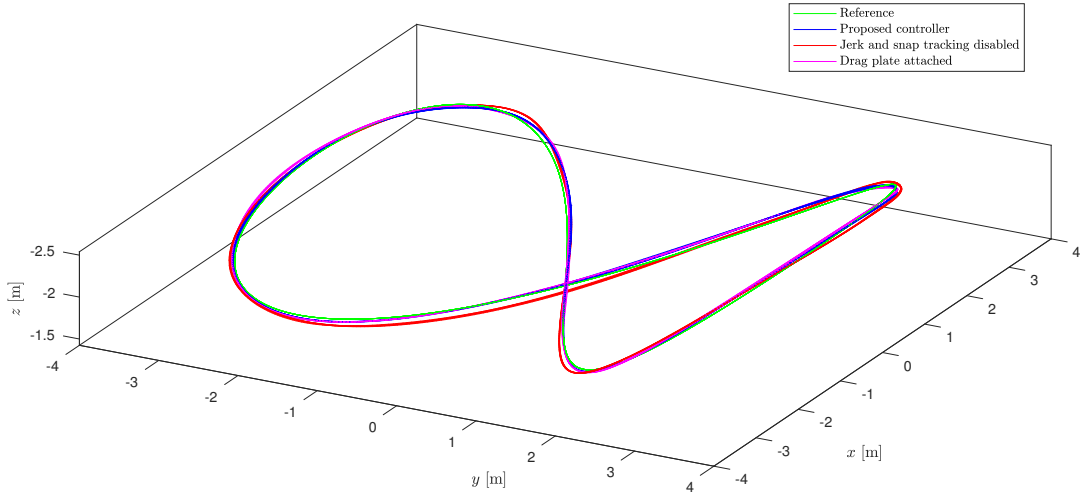


Fig. 15: Lemniscate trajectory for experiments with various configurations.

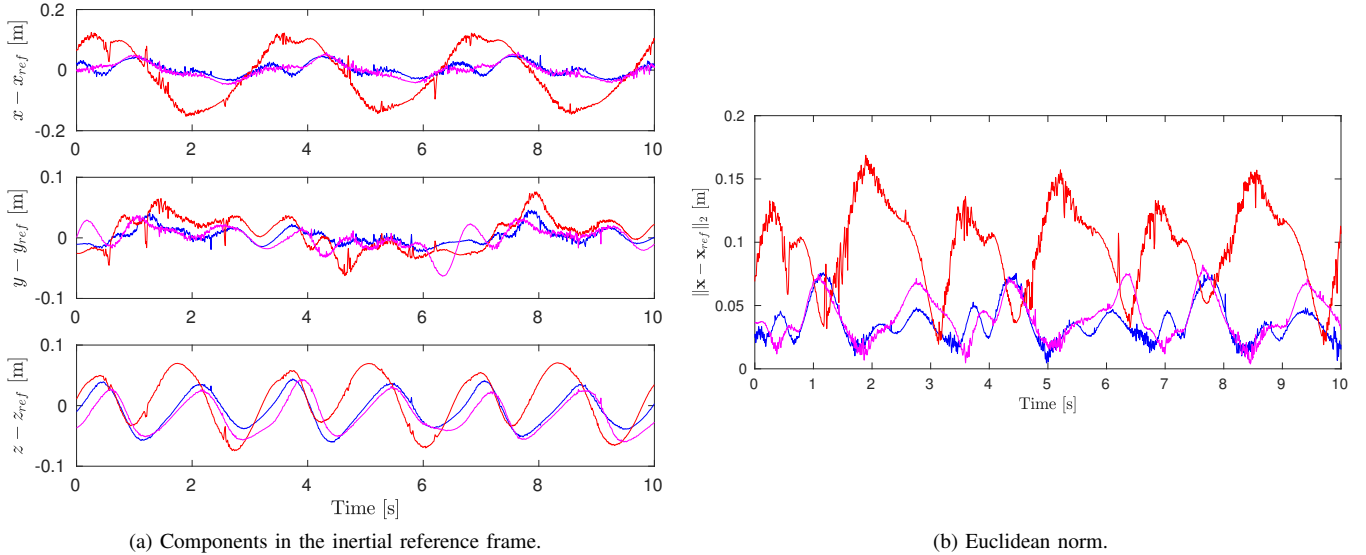


Fig. 16: Lemniscate trajectory position tracking error for the proposed controller (blue), without jerk and snap tracking (red), and with drag plate attached (magenta).

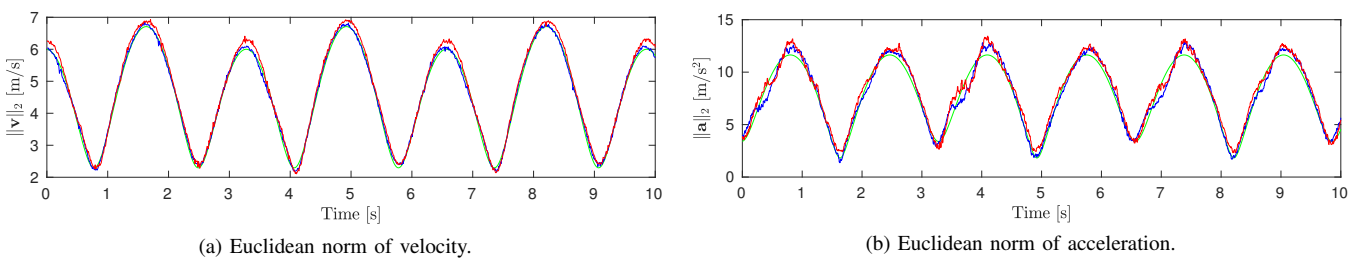


Fig. 17: Lemniscate trajectory Euclidean norm of velocity and acceleration for the reference trajectory (green), the proposed controller (blue), and jerk and snap tracking disabled (red).



Fig. 18: Quadrotor with $10 \text{ cm} \times 30 \text{ cm}$ cardboard drag plate.

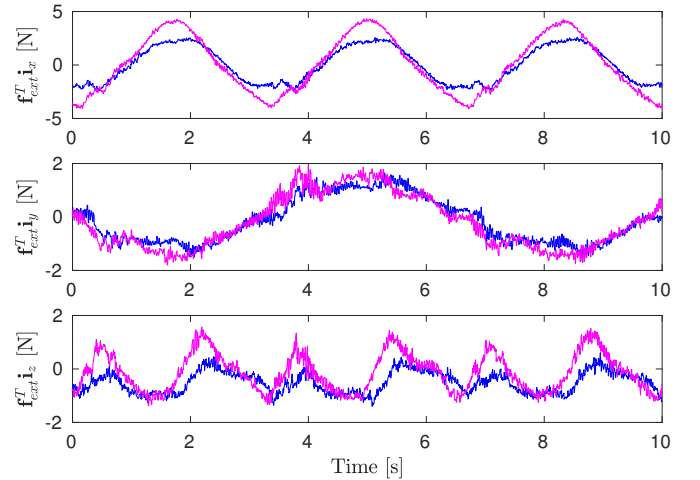


Fig. 19: Lemniscate trajectory estimated external disturbance force for the proposed controller using quadrotor without attached drag plate (blue), and with attached drag plate (magenta).

Therefore, nonlinear inversion of (39) — as described in Section III-E — theoretically results in improved tracking of the angular acceleration command and thereby improves trajectory tracking performance.

Comparison of columns (i) and (iv) in Table V shows that, in this case, a slight improvement was obtained by using nonlinear INDI angular acceleration control as derived in this paper. To fully determine the significance of the improvement, additional experiments on various trajectories are necessary. Position (error) and velocity data are not visualized for the linearized INDI controller, as these cannot clearly be distinguished from the curves for the nonlinear INDI controller.

F. Hover with Disturbance Force

For a constant σ_{ref} input, *i.e.*, hover, the controller achieves 0.7 cm RMS position tracking error if no external disturbance is purposely applied. In this section, we present results for hover with an external disturbance force through a tensioned wire. One end of the wire is attached to the bottom plate of the quadrotor. We pull on the other end of the wire to drag the vehicle away from its hover position.

In Fig. 20, it can be seen that the quadrotor maintains its position to within at most 6 cm, while a changing disturbance force is applied through the wire. The RMS position tracking error is 1.7 cm. The largest position error occurs when the wire is quickly released and the external force disappears.

Figure 21 shows the estimated external disturbance force, computed according to (21). The force component in the \mathbf{i}_z -direction has a small steady-state value due to discrepancy between true and estimated thrust. Comparison to Fig. 22 shows that the direction of the estimated external disturbance force vector corresponds to the direction of the wire. For example, at 7 s, Fig. 21 shows that the external force has a negative component in the \mathbf{i}_x -direction and a positive component in the \mathbf{i}_y -direction; and in Fig. 22(a) the wire

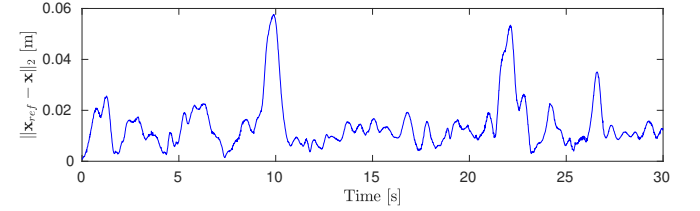


Fig. 20: Euclidean norm of position error during hover with disturbance force.

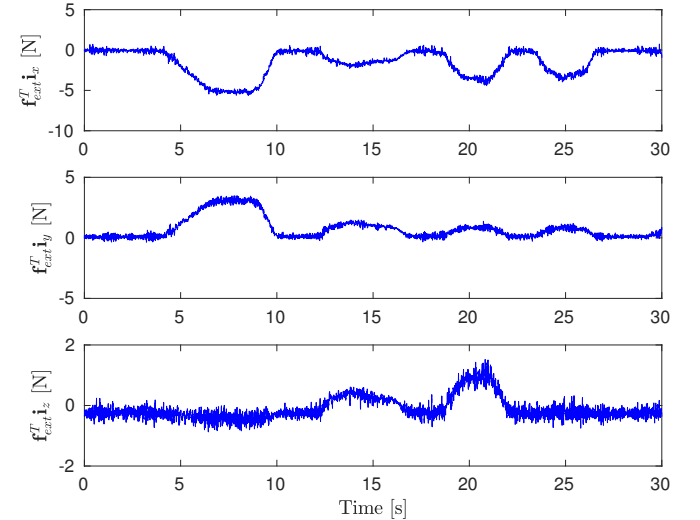


Fig. 21: Estimated external disturbance force during hover with disturbance force.

is indeed tensioned horizontally in negative \mathbf{i}_x - and positive \mathbf{i}_y -direction. The largest estimated external disturbance force occurs at 8.5 s, and amounts to 6.5 N.

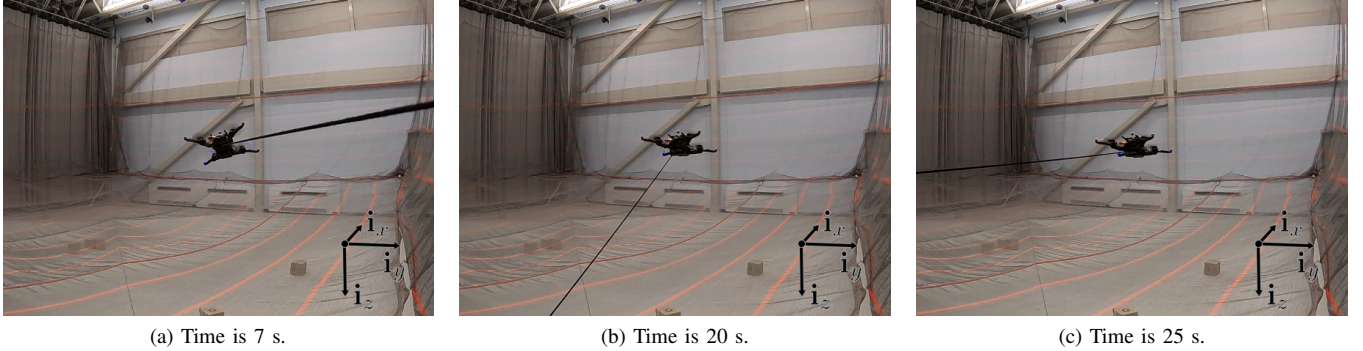


Fig. 22: Quadrotor in hover with external disturbance force through tensioned wire.

VI. CONCLUSIONS

In this paper, we studied the problem of designing control systems for the tracking of aggressive, *i.e.*, fast and agile, trajectories for quadrotor vehicles. We proposed a novel control system based on incremental nonlinear dynamic inversion and differential flatness to track position and yaw angle with their derivatives of up to fourth order, specifically, the position, velocity, acceleration, jerk, and snap along with the yaw angle, yaw rate and yaw acceleration. The tracking of reference snap was enabled by closed-loop control of the propeller speeds using optical encoders attached to each motor hub. The resulting control system achieves 4.0 cm RMS position tracking error in agile and fast flight, reaching a top speed of 8.2 m/s and acceleration of 2g, in a 6.5 m long, 6.5 m wide, and 1.5 m tall flight volume. Our analysis and experiments demonstrated the robustness of the control design against external disturbances, making it particularly suitable for high-speed flight where significant aerodynamic effects occur. The proposed controller does not require any modeling or estimation of aerodynamic drag parameters.

ACKNOWLEDGMENT

The authors thank Jasper Arneberg, Thomas Sayre-McCord, Varun Murali, and Winter Guerra, for help with the experiments. This work was supported in part by the Office of Naval Research (ONR) through grant N00014-17-1-2670.

REFERENCES

- [1] J.-J. E. Slotine and W. Li, *Applied nonlinear control*. Prentice Hall, Englewood Cliffs, 1991.
- [2] A. Isidori, *Nonlinear control systems*. Springer, New York, 1995.
- [3] S. Sastry, *Nonlinear systems: Analysis, stability, and control*. Springer-Verlag, New York, 1999.
- [4] S. A. Snell, D. F. Enns, and W. L. Garrard, “Nonlinear inversion flight control for a supermaneuverable aircraft,” *AIAA Journal of Guidance, Control, and Dynamics*, vol. 15, no. 4, pp. 976–984, 1992.
- [5] D. J. Bugajski and D. F. Enns, “Nonlinear control law with application to high angle-of-attack flight,” *AIAA Journal of Guidance, Control, and Dynamics*, vol. 15, no. 3, pp. 761–767, 1992.
- [6] J. Hauser, S. Sastry, and G. Meyer, “Nonlinear control design for slightly non-minimum phase systems: Application to V/STOL aircraft,” *Automatica*, vol. 28, no. 4, pp. 665–679, 1992.
- [7] D. F. Enns, D. J. Bugajski, R. Hendrick, and G. Stein, “Dynamic inversion: an evolving methodology for flight control design,” *International Journal of Control*, vol. 59, no. 1, pp. 71–91, 1994.
- [8] T. Koo and S. Sastry, “Output tracking control design of a helicopter model based on approximate linearization,” in *Decision and Control (CDC), 37th IEEE Conference on*, pp. 3635–3640, IEEE, 1998.
- [9] D. Lee, H. J. Kim, and S. Sastry, “Feedback linearization vs. adaptive sliding mode control for a quadrotor helicopter,” *International Journal of Control, Automation and Systems*, vol. 7, no. 3, pp. 419–428, 2009.
- [10] R. Xu and U. Ozguner, “Sliding mode control of a quadrotor helicopter,” in *Decision and Control (CDC), 45th IEEE Conference on*, pp. 4957–4962, IEEE, 2006.
- [11] T. Madani and A. Benallegue, “Backstepping sliding mode control applied to a miniature quadrotor flying robot,” in *Industrial Electronics (IECON), 32nd Annual Conference on*, pp. 700–705, IEEE, 2006.
- [12] E. Frazzoli, M. A. Dahleh, and E. Feron, “Trajectory tracking control design for autonomous helicopters using a backstepping algorithm,” in *American Control Conference (ACC)*, vol. 6, pp. 4102–4107, IEEE, 2000.
- [13] S. Sieberling, Q. Chu, and J. Mulder, “Robust flight control using incremental nonlinear dynamic inversion and angular acceleration prediction,” *AIAA Journal of Guidance, Control, and Dynamics*, vol. 33, no. 6, pp. 1732–1742, 2010.
- [14] P. Simplício, M. Pavel, E. Van Kampen, and Q. Chu, “An acceleration measurements-based approach for helicopter nonlinear flight control using incremental nonlinear dynamic inversion,” *Control Engineering Practice*, vol. 21, no. 8, pp. 1065–1077, 2013.
- [15] P. Smith, “A simplified approach to nonlinear dynamic inversion based flight control,” in *AIAA Atmospheric Flight Mechanics Conference*, pp. 4461–4469, AIAA, 1998.
- [16] B. Bacon and A. Ostroff, “Reconfigurable flight control using nonlinear dynamic inversion with a special accelerometer implementation,” in *AIAA Guidance, Navigation, and Control Conference and Exhibit*, pp. 4565–4579, AIAA, 2000.
- [17] E. J. Smeur, Q. P. Chu, and G. C. de Croon, “Adaptive incremental nonlinear dynamic inversion for attitude control of micro air vehicles,” *AIAA Journal of Guidance, Control, and Dynamics*, vol. 38, no. 12, pp. 450–461, 2015.
- [18] E. J. Smeur, G. C. de Croon, and Q. P. Chu, “Cascaded incremental nonlinear dynamic inversion control for MAV disturbance rejection,” *Control Engineering Practice*, vol. 73, pp. 79–90, 2018.
- [19] M. Fliess, J. Lévine, P. Martin, and P. Rouchon, “Sur les systèmes non linéaires différentiellement plats,” *CR Acad. Sci. Paris*, pp. 619–624, 1992.
- [20] P. Martin, *Contribution à l'étude des systèmes différentiellement plats*. Ph.D thesis, École Nationale Supérieure des Mines de Paris, 1992.
- [21] M. Van Nieuwstadt, M. Rathinam, and R. Murray, “Differential flatness and absolute equivalence of nonlinear control systems,” *SIAM Journal on Control and Optimization*, vol. 36, no. 4, pp. 1225–1239, 1998.
- [22] P. Martin, “Aircraft control using flatness,” in *Control, Optimization and Supervision, IMACS/IEEE-SMC Multiconference and CESA Symposium on*, pp. 194–199, IEEE, 1996.
- [23] G. Rivera and O. Sawodny, “Flatness-based tracking control and nonlinear observer for a micro aerial quadcopter,” in *Numerical Analysis and Applied Mathematics (ICNAAM), International Conference on*, pp. 386–389, American Institute of Physics, 2010.
- [24] J. Ferrin, R. Leishman, R. Beard, and T. McLain, “Differential flatness

- based control of a rotorcraft for aggressive maneuvers,” in *Intelligent Robots and Systems (IROS), IEEE/RSJ International Conference on*, pp. 2688–2693, IEEE, 2011.
- [25] T. Engelhardt, T. Konrad, B. Schäfer, and D. Abel, “Flatness-based control for a quadrotor camera helicopter using model predictive control trajectory generation,” in *Control and Automation (MED), 24th Mediterranean Conference on*, pp. 852–859, IEEE, 2016.
- [26] M. Faessler, A. Franchi, and D. Scaramuzza, “Differential flatness of quadrotor dynamics subject to rotor drag for accurate tracking of high-speed trajectories,” *IEEE Robotics and Automation Letters*, vol. 3, no. 2, pp. 620–626, 2018.
- [27] G. Hoffmann, D. G. Rajnarayanan, S. L. Waslander, D. Dostal, J. S. Jang, and C. J. Tomlin, “The Stanford testbed of autonomous rotorcraft for multi agent control (STARMAC),” in *Digital Avionics Systems Conference (DASC), The 23rd*, vol. 2, pp. 12.E.4.1–10, IEEE, 2004.
- [28] I. Kroo, F. Prinz, M. Shantz, P. Kunz, G. Fay, S. Cheng, T. Fabian, and C. Partridge, *The mesicopter: A miniature rotorcraft concept. Phase II interim report*. Stanford University, 2000.
- [29] P. Pounds, R. Mahony, P. Hynes, and J. M. Roberts, “Design of a four-rotor aerial robot,” in *Robotics and Automation (ACRA), Australasian Conference on*, pp. 145–150, Australian Robotics & Automation Association, 2002.
- [30] T. Hamel, R. Mahony, R. Lozano, and J. Ostrowski, “Dynamic modelling and configuration stabilization for an X4-flyer,” in *15th IFAC World Congress*, IFAC, 2002.
- [31] M. Valenti, B. Bethke, G. Fiore, J. How, and E. Feron, “Indoor multi-vehicle flight testbed for fault detection, isolation, and recovery,” in *AIAA Guidance, Navigation, and Control Conference and Exhibit*, p. 6200, AIAA, 2006.
- [32] J. P. How, B. Behnke, A. Frank, D. Dale, and J. Vian, “Real-time indoor autonomous vehicle test environment,” *IEEE Control Systems*, vol. 28, no. 2, pp. 51–64, 2008.
- [33] S. Zarovy, M. Costello, A. Mehta, G. Gremillion, D. Miller, B. Ranganathan, J. S. Humbert, and P. Samuel, “Experimental study of gust effects on micro air vehicles,” in *AIAA Atmospheric Flight Mechanics Conference*, pp. 7818–7844, AIAA, 2010.
- [34] G. Ducard and R. D’Andrea, “Autonomous quadrotor flight using a vision system and accommodating frames misalignment,” in *Industrial Embedded Systems (SIES), IEEE International Symposium on*, pp. 261–264, IEEE, 2009.
- [35] N. Michael, D. Mellinger, Q. Lindsey, and V. Kumar, “The GRASP multiple micro-UAV testbed,” *IEEE Robotics & Automation Magazine*, vol. 17, no. 3, pp. 56–65, 2010.
- [36] M. Ol, G. Parker, G. Abate, and J. Evers, “Flight controls and performance challenges for MAVs in complex environments,” in *AIAA Guidance, Navigation and Control Conference and Exhibit*, pp. 6508–6529, AIAA, 2008.
- [37] S. Bieniawski, D. Halaas, and J. Vian, “Micro-aerial vehicle flight in turbulent environments: Use of an indoor flight facility for rapid design and evaluation,” in *AIAA Guidance, Navigation and Control Conference and Exhibit*, pp. 6512–6522, AIAA, 2008.
- [38] D. Mellinger, N. Michael, and V. Kumar, “Trajectory generation and control for precise aggressive maneuvers with quadrotors,” *The International Journal of Robotics Research*, vol. 31, no. 5, pp. 664–674, 2012.
- [39] M. Müller, S. Lupashin, and R. D’Andrea, “Quadrocopter ball juggling,” in *Intelligent Robots and Systems (IROS), IEEE/RSJ International Conference on*, pp. 5113–5120, IEEE, 2011.
- [40] J. Svacha, K. Mohta, and V. Kumar, “Improving quadrotor trajectory tracking by compensating for aerodynamic effects,” in *Unmanned Aircraft Systems (ICUAS), International Conference on*, pp. 860–866, IEEE, 2017.
- [41] J.-M. Kai, G. Allibert, M.-D. Hua, and T. Hamel, “Nonlinear feedback control of quadrotors exploiting first-order drag effects,” in *20th IFAC World Congress*, vol. 50, pp. 8189–8195, IFAC, 2017.
- [42] H. Liu, D. Li, Z. Zuo, and Y. Zhong, “Robust three-loop trajectory tracking control for quadrotors with multiple uncertainties,” *IEEE Transactions on Industrial Electronics*, vol. 63, no. 4, pp. 2263–2274, 2016.
- [43] H. Huang, G. M. Hoffmann, S. L. Waslander, and C. J. Tomlin, “Aerodynamics and control of autonomous quadrotor helicopters in aggressive maneuvering,” in *Robotics and Automation (ICRA), IEEE International Conference on*, pp. 3277–3282, IEEE, 2009.
- [44] A. P. Schoellig, F. L. Mueller, and R. D’Andrea, “Optimization-based iterative learning for precise quadrocopter trajectory tracking,” *Autonomous Robots*, vol. 33, no. 1-2, pp. 103–127, 2012.
- [45] D. Mellinger and V. Kumar, “Minimum snap trajectory generation and control for quadrotors,” in *Robotics and Automation (ICRA), IEEE International Conference on*, pp. 2520–2525, IEEE, 2011.
- [46] M. Bronz and S. Karaman, “Preliminary experimental investigation of small scale propellers at high incidence angle,” in *AIAA Aerospace Sciences Meeting*, pp. 1268–1277, AIAA, 2018.

APPENDIX I DERIVATION OF DIFFERENTIAL FLATNESS PROPERTIES

In Section II-B, we show how differential flatness is used to compute feedforward control inputs based on the reference trajectory and its derivatives. A more in-depth look at the differential flatness property of the quadrotor dynamics and a full derivation of the results used in the trajectory tracking control are given in this appendix.

Similar to [45], we consider a four-dimensional reference trajectory function

$$\sigma_{ref}(t) = [\mathbf{x}_{ref}(t)^T \ \psi_{ref}(t)]^T, \quad (81)$$

consisting of the quadrotor position in the inertial reference frame $\mathbf{x}_{ref}(t) \in \mathbb{R}^3$, and the vehicle yaw angle $\psi_{ref}(t) \in \mathbb{T}$, where \mathbb{T} denotes the circle group. For convenience of notation, we do not explicitly write the time argument t everywhere. We assume that \mathbf{x}_{ref} is of differentiability class C^4 , i.e., its first four derivatives exist and are continuous, and that ψ_{ref} is of class C^2 . In this appendix, we distinguish between state variables and trajectory references by using the subscript ref only for (elements of) the reference trajectory function σ_{ref} and its derivatives. Only in the main body of the article, the subscript ref is also used for state variable references that are derived from the trajectory function, as described in Section II-B.

In this appendix, we consider the quadrotor dynamics given by (1) to (4), with

$$\begin{bmatrix} \mu \\ T \end{bmatrix} = \mathbf{G}_1 \boldsymbol{\omega}^{o2}. \quad (82)$$

Here, we designate the motor speed vector $\boldsymbol{\omega}$ as the input of the system of differential equations. For the control design in the main body of this paper, we consider a more elaborate model that includes contributions by the motor speed derivative $\dot{\boldsymbol{\omega}}$, and we take into account closed-loop control of the motor speed. However, for the purpose of deriving the differential flatness properties, the simplified model suffices.

According to the differential flatness property of the quadrotor vehicle dynamics, all state variables, i.e., \mathbf{x} , \mathbf{v} , ξ and Ω , and the control input, i.e., $\boldsymbol{\omega}$, can be expressed as a function of σ_{ref} and its derivatives. By successive differentiation of the reference trajectory function, we can intuitively expose the connections between the trajectory (derivatives), and the state variables and control input.

- The trajectory component \mathbf{x}_{ref} directly prescribes \mathbf{x} .
- The first derivative of \mathbf{x}_{ref} , i.e., the reference velocity $\mathbf{v}_{ref} = \dot{\mathbf{x}}_{ref}$, is directly linked to the state \mathbf{v} .
- The second derivative of \mathbf{x}_{ref} , i.e., the reference acceleration $\mathbf{a}_{ref} = \ddot{\mathbf{x}}_{ref}$, is connected to the orientation and

TABLE VI: Differential flatness relations of state and input variables to reference trajectory function and its derivatives.

| State and input variables | Trajectory references |
|---------------------------|---|
| \mathbf{x} | \mathbf{x}_{ref} |
| \mathbf{v} | \mathbf{v}_{ref} |
| $\boldsymbol{\xi}$ | $\mathbf{a}_{ref}, \psi_{ref}$ |
| $\boldsymbol{\Omega}$ | $\mathbf{j}_{ref}, \psi_{ref}$ |
| $\boldsymbol{\omega}$ | $\mathbf{a}_{ref}, \mathbf{s}_{ref}, \ddot{\psi}_{ref}$ |

magnitude of the specific force vector that applies to the vehicle. Therefore \mathbf{a}_{ref} determines the thrust T , and the vehicle roll and pitch angles. The third component of $\boldsymbol{\xi}$, *i.e.*, the vehicle yaw angle, is given directly by ψ_{ref} .

- The third derivative of \mathbf{x}_{ref} , *i.e.*, the reference jerk $\mathbf{j}_{ref} = \ddot{\mathbf{x}}_{ref}$, is the rate of change of the reference acceleration. Hence it is related to the rate of change of the specific force vector magnitude and orientation. Consequently, the angular rate $\boldsymbol{\Omega}$ is determined by \mathbf{j}_{ref} and the first derivative of the reference yaw, $\dot{\psi}_{ref}$.
- The fourth derivative of \mathbf{x}_{ref} , *i.e.*, the reference snap $\mathbf{s}_{ref} = \dddot{\mathbf{x}}_{ref}$, is the second derivative of the acceleration and is thus linked to the second derivative of the specific force vector magnitude and orientation. Therefore the angular acceleration $\dot{\boldsymbol{\Omega}}$ is determined by \mathbf{s}_{ref} and the second derivative of the yaw reference, $\ddot{\psi}_{ref}$. The angular acceleration is a function of the three-dimensional moment vector $\boldsymbol{\mu}$ acting on the vehicle. As mentioned above, total thrust is connected to \mathbf{a}_{ref} , so that the four-dimensional motor speed vector $\boldsymbol{\omega}$ is fully determined by \mathbf{s}_{ref} , $\dot{\psi}_{ref}$, and \mathbf{a}_{ref} .

The connections given above are summarized in Table VI.

In the remainder of this appendix, we show mathematically how the state variables and control input can be obtained from the reference trajectory and its derivatives. The proposed control design — described in the main body of this paper — tracks the reference trajectory jerk and snap through feedforward attitude rate and attitude acceleration inputs, respectively. Therefore, we also show how the attitude rate and attitude acceleration are obtained from the reference trajectory.

A. Position, Velocity, and Attitude

The following states are directly obtained from the reference and its first derivative:

$$\mathbf{x} = \mathbf{x}_{ref} \quad (83)$$

$$\mathbf{v} = \mathbf{v}_{ref} \quad (84)$$

$$\psi = \psi_{ref} \quad (85)$$

Next, we equate the acceleration to the specific force acting on the vehicle:

$$\mathbf{a}_{ref} = g\mathbf{i}_z + \tau\mathbf{b}_z + m^{-1}\mathbf{f}_{ext}. \quad (86)$$

By rewriting (86), we obtain the following expression for the specific thrust vector in the inertial reference frame:

$$\begin{aligned} \tau\mathbf{b}_z &= \tau \begin{bmatrix} s\psi s\phi + c\psi s\theta c\phi \\ -c\psi s\phi + s\psi s\theta c\phi \\ c\theta c\phi \end{bmatrix} \\ &= \mathbf{a}_{ref} - g\mathbf{i}_z - m^{-1}\mathbf{f}_{ext}, \end{aligned} \quad (87)$$

where the first equality follows from the definition of \mathbf{b}_z , and c and s denote cos and sin, respectively. We consider the external force as a known constant in this appendix.

By (85), ψ is directly obtained from ψ_{ref} , so that we can solve for the remaining three unknown variables τ , ϕ , and θ . Since \mathbf{R} is orthonormal, we obtain the specific thrust as follows:

$$\tau = -\|\mathbf{a}_{ref} - g\mathbf{i}_z - m^{-1}\mathbf{f}_{ext}\|_2 \quad (88)$$

with the sign due to the convention that τ is positive in the direction \mathbf{b}_z . The total thrust is then obtained as

$$T = m\tau. \quad (89)$$

We note that the thrust vector is aligned with the \mathbf{b}_z -axis, so that ϕ and θ can be obtained geometrically, as follows. We rotate the inertial xz -plane to correct for the yaw angle ψ . The rotated plane is denoted xz_ψ , so that $xz_\psi = \text{span}(\mathbf{b}_x, \mathbf{i}_z)$. We assume the singular condition $\theta = \pm\frac{\pi}{2}$ does not hold. To compute the roll angle, we look at the thrust component $\text{proj}_{\perp xz_\psi}(\tau\mathbf{b}_z)$, which is perpendicular to the plane xz_ψ , and compare it to the total thrust magnitude. The ratio of these values is equal to $\sin\phi$, so that we obtain the roll angle as follows:

$$\phi = \arcsin \left(\frac{\tau\mathbf{b}_z^T(\mathbf{i}_x \sin \psi_{ref} - \mathbf{i}_y \cos \psi_{ref})}{\|\tau\mathbf{b}_z\|_2} \right). \quad (90)$$

If we project $\tau\mathbf{b}_z$ onto xz_ψ , then $\tan\theta$ is equal to the ratio of the magnitude of the horizontal and vertical components of the projected vector, *i.e.*, $\|\text{proj}_{xz_\psi}(\tau\mathbf{b}_z) \times \mathbf{i}_z\|_2$ and $(\tau\mathbf{b}_z)^T \mathbf{i}_z$, so that we can obtain the pitch angle as follows:

$$\theta = \arctan \left(\frac{\tau\mathbf{b}_z^T(\mathbf{i}_x \cos \psi_{ref} + \mathbf{i}_y \sin \psi_{ref})}{\tau\mathbf{b}_z^T \mathbf{i}_z} \right). \quad (91)$$

The attitude state vector $\boldsymbol{\xi}$ is obtained by combining (85), (90), and (91).

B. Attitude Rate, and Angular Rate

We take the temporal derivative of (86), which gives (92). In this equation, the yaw rate is directly obtained as $\dot{\psi} = \dot{\psi}_{ref}$ and the matrix \mathbf{C} is full rank if $\tau \neq 0$. Hence, $\dot{\phi}$, $\dot{\theta}$, $\dot{\tau}$ are uniquely defined and can be obtained as:

$$\begin{bmatrix} \dot{\phi} \\ \dot{\theta} \\ \dot{\tau} \end{bmatrix} = \mathbf{C}^{-1} (\mathbf{j}_{ref} - \dot{\psi}\mathbf{d}), \quad (93)$$

$$\begin{aligned}
\mathbf{j}_{ref} &= \frac{d}{dt} (g\mathbf{i}_z + \tau\mathbf{b}_z + m^{-1}\mathbf{f}_{ext}) \\
&= \tau\dot{\mathbf{R}}\mathbf{i}_z + \dot{\tau}\mathbf{b}_z \\
&= \tau\mathbf{R}[\Omega]_x\mathbf{i}_z + \dot{\tau}\mathbf{b}_z \\
&= \tau\mathbf{R}[\mathbf{i}_z]^T\mathbf{S}^{-1}\dot{\boldsymbol{\xi}} + \dot{\tau}\mathbf{b}_z \\
&= \tau \begin{bmatrix} c\phi s\psi - c\psi s\phi s\theta & c\phi c\psi c\theta & c\psi s\phi - c\phi s\psi s\theta \\ -c\phi c\psi - s\phi s\psi s\theta & c\phi c\theta s\psi & s\phi s\psi + c\phi c\psi s\theta \\ -c\theta s\phi & -c\phi s\theta & 0 \end{bmatrix} \begin{bmatrix} \dot{\phi} \\ \dot{\theta} \\ \dot{\psi} \end{bmatrix} + \dot{\tau} \begin{bmatrix} s\psi s\phi + c\psi s\theta c\phi \\ -c\psi s\phi + s\psi s\theta c\phi \\ c\theta c\phi \end{bmatrix} \\
&= \begin{bmatrix} \tau(c\phi s\psi - c\psi s\phi s\theta) & \tau c\phi c\psi c\theta & s\psi s\phi + c\psi s\theta c\phi \\ -\tau(c\phi c\psi + s\phi s\psi s\theta) & \tau c\phi c\theta s\psi & -c\psi s\phi + s\psi s\theta c\phi \\ -\tau c\theta s\phi & -\tau c\phi s\theta & c\theta c\phi \end{bmatrix} \begin{bmatrix} \dot{\phi} \\ \dot{\theta} \\ \dot{\tau} \end{bmatrix} + \dot{\psi} \begin{bmatrix} \tau(c\psi s\phi - c\phi s\psi s\theta) \\ \tau(s\phi s\psi + c\phi c\psi s\theta) \\ 0 \end{bmatrix} \\
&= \mathbf{C} \begin{bmatrix} \dot{\phi} \\ \dot{\theta} \\ \dot{\tau} \end{bmatrix} + \dot{\psi} \mathbf{d}
\end{aligned} \tag{92}$$

which results in the following expression for the attitude rate:

$$\dot{\boldsymbol{\xi}} = \begin{bmatrix} \dot{\phi} \\ \dot{\theta} \\ \dot{\psi} \end{bmatrix} = \frac{1}{\tau} \begin{bmatrix} -\mathbf{b}_y^T \\ \mathbf{b}_x^T / \cos \phi \\ 0 \end{bmatrix} \mathbf{j}_{ref} + \dot{\psi}_{ref} \begin{bmatrix} \sin \theta \\ -\cos \theta \tan \phi \\ 1 \end{bmatrix}. \tag{94}$$

The angular rate in the body reference frame Ω can now be obtained using the transformation

$$\Omega = \mathbf{S}^{-1}\dot{\boldsymbol{\xi}} \tag{95}$$

with

$$\mathbf{S}^{-1} = \begin{bmatrix} 1 & 0 & -\sin \theta \\ 0 & \cos \phi & \cos \theta \sin \phi \\ 0 & -\sin \phi & \cos \phi \cos \theta \end{bmatrix}. \tag{96}$$

The expression for $\dot{\tau}$ from 93 is not used here, since the system input is defined as ω . Comparison of the thrust derivative $\dot{\tau}$ to the motor rise time may however be useful to determine the dynamic feasibility of the trajectory.

C. Attitude Acceleration, and Angular Acceleration

In order to obtain an expression for the angular acceleration $\dot{\Omega}$, we first derive an expression for the attitude acceleration $\ddot{\boldsymbol{\xi}}$. We take the derivative of (92) to obtain:

$$\begin{aligned}
\mathbf{s}_{ref} &= \frac{d}{dt} (\tau\mathbf{R}[\mathbf{i}_z]^T\Omega + \dot{\tau}\mathbf{b}_z) \\
&= \dot{\tau}\mathbf{R}[\mathbf{i}_z]^T\Omega + \tau\mathbf{R}[\Omega]_x[\mathbf{i}_z]^T\Omega + \tau\mathbf{R}[\mathbf{i}_z]^T\dot{\Omega} \\
&\quad + \ddot{\tau}\mathbf{b}_z + \dot{\tau}\mathbf{R}[\mathbf{i}_z]^T\Omega \\
&= \mathbf{R}(\ddot{\tau}\mathbf{i}_z + (2\dot{\tau} + \tau[\Omega]_x)[\mathbf{i}_z]^T\Omega + \tau[\mathbf{i}_z]^T\dot{\Omega})
\end{aligned} \tag{97}$$

and we take the derivative of (95) to obtain:

$$\dot{\Omega} = -\mathbf{S}^{-1}\dot{\mathbf{S}}\Omega + \mathbf{S}^{-1}\ddot{\boldsymbol{\xi}}, \tag{98}$$

where

$$\dot{\mathbf{S}} = \dot{\phi} \begin{bmatrix} 0 & c\phi t\theta & -s\phi t\theta \\ 0 & -s\phi & -c\phi \\ 0 & \frac{c\phi}{\cos \theta} & -\frac{s\phi}{\cos \theta} \end{bmatrix} + \dot{\theta} \begin{bmatrix} 0 & -\frac{s\phi}{s^2\theta - 1} & \frac{c\phi}{c^2\theta} \\ 0 & 0 & 0 \\ 0 & -\frac{s\phi s\theta}{s^2\theta - 1} & \frac{c\phi s\theta}{c^2\theta} \end{bmatrix} \tag{99}$$

with t denoting tan. Substitution of (98) into (97) gives (100). In (100), the yaw acceleration is directly obtained as $\ddot{\psi} = \ddot{\psi}_{ref}$ and the matrix \mathbf{C} is full rank if $\tau \neq 0$, so $\ddot{\phi}, \ddot{\theta}, \ddot{\tau}$ are uniquely defined and can be obtained as:

$$\begin{bmatrix} \ddot{\phi} \\ \ddot{\theta} \\ \ddot{\tau} \end{bmatrix} = \mathbf{C}^{-1} (\mathbf{s}_{ref} - \ddot{\psi} \mathbf{d} - \mathbf{e}), \tag{101}$$

which results in the following expression for the attitude acceleration:

$$\begin{aligned}
\ddot{\boldsymbol{\xi}} &= \begin{bmatrix} \ddot{\phi} \\ \ddot{\theta} \\ \ddot{\psi} \end{bmatrix} = \frac{1}{\tau} \begin{bmatrix} -\mathbf{b}_y^T \\ \mathbf{b}_x^T / \cos \phi \\ 0 \end{bmatrix} \mathbf{s}_{ref} \\
&\quad + \ddot{\psi}_{ref} \begin{bmatrix} \sin \theta \\ -\cos \theta \tan \phi \\ 1 \end{bmatrix} - \begin{bmatrix} 1 & 0 & 0 \\ 0 & 1 & 0 \\ 0 & 0 & 0 \end{bmatrix} \mathbf{C}^{-1} \mathbf{e}.
\end{aligned} \tag{102}$$

The body-fixed angular acceleration $\dot{\Omega}$ is can now be obtained using (98). Similar to $\dot{\tau}$, the expression for $\ddot{\tau}$ is not used, since the system input is defined as ω .

D. Motor Speeds

At this point, we have obtained state variables $\mathbf{x}, \mathbf{v}, \boldsymbol{\xi}$ and Ω in terms of the trajectory reference. Moreover, we derived the expressions for attitude rate $\dot{\boldsymbol{\xi}}$ and attitude acceleration $\ddot{\boldsymbol{\xi}}$ that are used to compute feedforward control inputs, as shown in Section II-B. For the sake of completeness, we complete the derivation in this appendix to show how the input vector ω is a function of the thrust as obtained in (89) and the control moment μ .

$$\begin{aligned}
\mathbf{s}_{ref} &= \tau \mathbf{R} [\mathbf{i}_z]_{\times}^T \mathbf{S}^{-1} \ddot{\boldsymbol{\xi}} + \ddot{\tau} \mathbf{b}_z + \mathbf{R} \left((2\dot{\tau} + \tau [\boldsymbol{\Omega}]_{\times}) [\mathbf{i}_z]_{\times}^T \boldsymbol{\Omega} - \tau [\mathbf{i}_z]_{\times}^T \mathbf{S}^{-1} \dot{\boldsymbol{\Omega}} \right) \\
&= \tau \begin{bmatrix} c\phi s\psi - c\psi s\phi s\theta & c\phi c\psi c\theta & c\psi s\phi - c\phi s\psi s\theta \\ -c\phi c\psi - s\phi s\psi s\theta & c\phi c\theta s\psi & s\phi s\psi + c\phi c\psi s\theta \\ -c\theta s\phi & -c\phi s\theta & 0 \end{bmatrix} \begin{bmatrix} \ddot{\phi} \\ \ddot{\theta} \\ \ddot{\psi} \end{bmatrix} + \ddot{\tau} \begin{bmatrix} s\psi s\phi + c\psi s\theta c\phi \\ -c\psi s\phi + s\psi s\theta c\phi \\ c\theta c\phi \end{bmatrix} \\
&\quad + \mathbf{R} \left((2\dot{\tau} + \tau [\boldsymbol{\Omega}]_{\times}) [\mathbf{i}_z]_{\times}^T \boldsymbol{\Omega} - \tau [\mathbf{i}_z]_{\times}^T \mathbf{S}^{-1} \dot{\boldsymbol{\Omega}} \right) \quad (100) \\
&= \begin{bmatrix} \tau (c\phi s\psi - c\psi s\phi s\theta) & \tau c\phi c\psi c\theta & s\psi s\phi + c\psi s\theta c\phi \\ -\tau (c\phi c\psi + s\phi s\psi s\theta) & \tau c\phi c\theta s\psi & -c\psi s\phi + s\psi s\theta c\phi \\ -\tau c\theta s\phi & -\tau c\phi s\theta & c\theta c\phi \end{bmatrix} \begin{bmatrix} \ddot{\phi} \\ \ddot{\theta} \\ \ddot{\tau} \end{bmatrix} + \ddot{\psi} \begin{bmatrix} \tau (c\psi s\phi - c\phi s\psi s\theta) \\ \tau (s\phi s\psi + c\phi c\psi s\theta) \\ 0 \end{bmatrix} \\
&\quad + \mathbf{R} \left((2\dot{\tau} + \tau [\boldsymbol{\Omega}]_{\times}) [\mathbf{i}_z]_{\times}^T \boldsymbol{\Omega} - \tau [\mathbf{i}_z]_{\times}^T \mathbf{S}^{-1} \dot{\boldsymbol{\Omega}} \right) \\
&= \mathbf{C} \begin{bmatrix} \ddot{\phi} \\ \ddot{\theta} \\ \ddot{\tau} \end{bmatrix} + \ddot{\psi} \mathbf{d} + \mathbf{e}
\end{aligned}$$

First, we rewrite the angular dynamics equation (4) to obtain the following expression for the control moment:

$$\boldsymbol{\mu} = \mathbf{J} \dot{\boldsymbol{\Omega}} - \boldsymbol{\mu}_{ext} + \boldsymbol{\Omega} \times \mathbf{J} \boldsymbol{\Omega}. \quad (103)$$

Similar to \mathbf{f}_{ext} , we consider $\boldsymbol{\mu}_{ext}$ a known constant. Since $\boldsymbol{\omega}$ is considered the instantaneous input of the system, it can be obtained by the following inversion of (82):

$$\boldsymbol{\omega} = \left(\mathbf{G}_1^{-1} \begin{bmatrix} \boldsymbol{\mu} \\ T \end{bmatrix} \right)^{\circ \frac{1}{2}} \quad (104)$$

with \mathbf{G}_1 according to (8), and the thrust and control moment obtained from (89) and (103), respectively.

In the main body of this paper, we also consider the effect of the motor speed rate of change $\dot{\boldsymbol{\omega}}$, *i.e.*, the second term of (7), by numerically estimating $\dot{\boldsymbol{\omega}}$ based on the difference between current and commanded motor speed values, as shown in Section III-E. Furthermore, the control moment $\boldsymbol{\mu}$ is calculated in a different manner in the control design; its purpose is not only to track the trajectory snap, but also to control the attitude and attitude rate, as described in Section III-C and Appendix II.

APPENDIX II

DERIVATION OF NONLINEAR DYNAMICS INVERSION OF ATTITUDE DYNAMICS

Section III-C presents the attitude control design based on NDI. In this appendix, we show the derivation of the corresponding linear system and control mapping based on Lie derivatives. NDI, or feedback linearization, of the angular kinematics allows us to obtain a controller that takes into account nonlinear angular dynamics, but that can be tuned using linear techniques such as pole placement and LQR. This controller does not incur the robustness issues commonly associated with NDI, since the feedback linearization only involves angular kinematics without taking into account any model-specific parameters.

The first Lie derivative of the vector-valued function h with respect to the vector field f at the point χ is defined as

$$L_f h(\chi) = \frac{\partial h(\chi)}{\partial \chi} f(\chi), \quad (105)$$

and successive Lie derivatives are defined by the recursion

$$L_f^n h(\chi) = L_f L_f^{n-1} h(\chi) = \frac{\partial L_f^{n-1} h(\chi)}{\partial \chi} f(\chi). \quad (106)$$

We consider the state vector

$$\chi = \begin{bmatrix} \boldsymbol{\xi} \\ \boldsymbol{\Omega} \end{bmatrix}, \quad (107)$$

where $\boldsymbol{\xi} = [\phi \ \theta \ \psi]^T$ is the roll-pitch-yaw Euler attitude vector, and $\boldsymbol{\Omega} = [p \ q \ r]^T$ is the angular velocity vector in the body-fixed reference frame. The state dynamics are given by

$$\dot{\chi} = f(\chi) + g(\chi) \dot{\boldsymbol{\Omega}} = \underbrace{\begin{bmatrix} \mathbf{S} \boldsymbol{\Omega} \\ \mathbf{0}_{3 \times 1} \end{bmatrix}}_{f(\chi)} + \underbrace{\begin{bmatrix} \mathbf{0}_{3 \times 3} \\ \mathbf{I} \end{bmatrix}}_{g(\chi)} \dot{\boldsymbol{\Omega}}, \quad (108)$$

where $\dot{\boldsymbol{\Omega}}$ denotes the vehicle angular acceleration in the body-fixed reference frame and \mathbf{S} denotes the following transformation matrix:

$$\mathbf{S} = \begin{bmatrix} 1 & \sin \phi \tan \theta & \cos \phi \tan \theta \\ 0 & \cos \phi & -\sin \phi \\ 0 & \frac{\sin \phi}{\cos \theta} & \frac{\cos \phi}{\cos \theta} \end{bmatrix}. \quad (109)$$

The output function h is defined as

$$h(\chi) = \boldsymbol{\xi}. \quad (110)$$

For the NDI attitude controller described in this appendix, we do not consider the complete angular dynamics equations as given by (3) and (4). As shown in (108), we consider the body-frame angular acceleration $\dot{\boldsymbol{\Omega}}$ as the input of the state dynamics equation, and do not consider the control moment $\boldsymbol{\mu}$ and external moment $\boldsymbol{\mu}_{ext}$. This has two major advantages. Firstly, the NDI controller does not incur the issues due

to model mismatches that are typical for inversion-based controllers, because it does not take into account the vehicle inertia matrix \mathbf{J} or any other model-specific parameters. Secondly, the external moment μ_{ext} is not included in the model-based NDI equations, but instead considered when the control moment μ is determined incrementally by the INDI controller described in Section III-D. This further improves controller robustness against modeling discrepancies.

The relative degree of the system consisting of dynamics equation (108) and output equation (110) is said to be equal to d on the domain \mathcal{D} if

$$L_g L_f^n h(\chi) = 0 \quad \forall \chi \in \mathcal{D} \text{ and all } n \leq d-2, \quad (111)$$

$$L_g L_f^{d-1} h(\chi) \neq 0. \quad (112)$$

In other words, the relative degree equals the number of times the output function must be differentiated for the control input to appear in the expression. It is determined by taking Lie derivatives:

$$L_g h(\chi) = [\mathbf{I} \quad \mathbf{0}_{3 \times 3}] \begin{bmatrix} \mathbf{0}_{3 \times 3} \\ \mathbf{I} \end{bmatrix} = \mathbf{0}, \quad (113)$$

and

$$L_f h(\chi) = \mathbf{S}\Omega \quad (114)$$

so that

$$L_g L_f h(\chi) = \frac{\partial \mathbf{S}\Omega}{\partial \chi} g(\chi) = \left[\frac{\partial \mathbf{S}\Omega}{\partial \xi} \quad \mathbf{S} \right] \begin{bmatrix} \mathbf{0}_{3 \times 3} \\ \mathbf{I} \end{bmatrix} = \mathbf{S} \neq \mathbf{0}, \quad (115)$$

which gives $d = 2$ for all χ , by (111) and (112). We use the Lie derivative up to degree $d-1$ to transform the state to the normal form:

$$\eta = \begin{bmatrix} \xi \\ \dot{\xi} \end{bmatrix} = \begin{bmatrix} h(\chi) \\ L_f h(\chi) \end{bmatrix} = \begin{bmatrix} \xi \\ \mathbf{S}\Omega \end{bmatrix}, \quad (116)$$

which is a diffeomorphism on $\{\chi | \theta \neq \pm \frac{\pi}{2}\}$, so that on this set the evolution of the transformed state is given by

$$\dot{\eta} = \begin{bmatrix} \xi \\ L_f^2 h(\chi) + L_g L_f h(\chi) \dot{\Omega} \end{bmatrix}. \quad (117)$$

By setting

$$\dot{\Omega} = (L_g L_f h(\chi))^{-1} (\bar{u} - L_f^2 h(\chi)), \quad (118)$$

we obtain a double integrator system

$$\dot{\eta} = \begin{bmatrix} \mathbf{0}_{3 \times 3} & \mathbf{I} \\ \mathbf{0}_{3 \times 3} & \mathbf{0}_{3 \times 3} \end{bmatrix} \eta + \begin{bmatrix} \mathbf{0}_{3 \times 3} \\ \mathbf{I} \end{bmatrix} \bar{u} \quad (119)$$

or, equivalently,

$$\ddot{\xi} = \bar{u} \quad (120)$$

with \bar{u} a *fictitious* control input. Control design for (120) can be done using linear techniques, resulting in a control law of the form

$$\mathbf{u} = \mathbf{K}_\eta (\eta_c - \eta) = \mathbf{K}_\eta \begin{bmatrix} \xi_c - \xi \\ \dot{\xi}_{ref} - \mathbf{S}\Omega \end{bmatrix}, \quad (121)$$

where \mathbf{K}_η is a 3×6 gain matrix, and $\eta_c = [\xi_c^T \quad \dot{\xi}_{ref}^T]^T$ contains the attitude command obtained from the linear acceleration control loop (see Section III-B) and the reference attitude rate obtained from the trajectory reference function, as described in Section II-B and Appendix I. The control \mathbf{u} nulls the state deviation $\eta_c - \eta$. To improve tracking performance for a time-variant command vector, we add the reference attitude acceleration $\ddot{\xi}_{ref}$ directly to \mathbf{u} , as follows:

$$\bar{u} = u + \ddot{\xi}_{ref}. \quad (122)$$

The new control \bar{u} anticipates the future value of η_c through the second term of (122) and thereby has improved tracking performance. The addition of the terms in (122) is permitted by linearity of (120).

The body-fixed angular acceleration command can now be obtained by substitution of (121) and (122) into (118), as follows:

$$\begin{aligned} \dot{\Omega}_c &= (L_g L_f h(\chi))^{-1} \left(\mathbf{K}_\eta \begin{bmatrix} \xi_c - \xi \\ \dot{\xi}_{ref} - \mathbf{S}\Omega \end{bmatrix} + \ddot{\xi}_{ref} - L_f^2 h(\chi) \right) \\ &= \mathbf{S}^{-1} \left(\mathbf{K}_\eta \begin{bmatrix} \xi_c - \xi \\ \dot{\xi}_{ref} - \mathbf{S}\Omega \end{bmatrix} + \ddot{\xi}_{ref} - L_f^2 h(\chi) \right), \end{aligned} \quad (123)$$

where

$$\mathbf{S}^{-1} = \begin{bmatrix} 1 & 0 & -\sin \theta \\ 0 & \cos \phi & \cos \theta \sin \phi \\ 0 & -\sin \phi & \cos \phi \cos \theta \end{bmatrix} \quad (124)$$

and

$$\begin{aligned} L_f^2 h(\chi) &= \frac{\partial \mathbf{S}\Omega}{\partial \chi} f(\chi) \\ &= \left[\frac{\partial \mathbf{S}\Omega}{\partial \xi} \quad \mathbf{S} \right] \begin{bmatrix} \mathbf{S}\Omega \\ \mathbf{0}_{3 \times 3} \end{bmatrix} \\ &= \begin{bmatrix} \frac{s\theta(qc\phi - rs\phi)}{c\theta} & \frac{rc\phi + qs\phi}{c^2\theta} & 0 \\ -rc\phi - qs\phi & 0 & 0 \\ \frac{qc\phi - rs\phi}{c\theta} & \frac{s\theta(rc\phi + qs\phi)}{c^2\theta} & 0 \end{bmatrix} \\ &\quad \begin{bmatrix} p + rc\phi t\theta + qs\phi t\theta \\ qc\phi - rs\phi \\ \frac{rc\phi + qs\phi}{c\theta} \end{bmatrix} \end{aligned} \quad (125)$$

with c , s , and t denoting \cos , \sin , and \tan , respectively.